Dissertation
submitted to the
Combined Faculties for the Natural Sciences and for Mathematics
of the Ruperto-Carola University of Heidelberg, Germany
for the degree of
Doctor of Natural Sciences

Submitted by
Brian Robert Rankin
born in Redwood City, California, USA

Oral examination: November 24th, 2010

Stimulated Emission Depletion Microscopy with Stimulated Raman Scattering Light Sources

Referees:
Prof. Stefan W. Hell
Prof. Dirk Dubbers

Abstract. Light sources offering a spectrally flexible output in the yellow-orange region of the visible spectrum are of great interest for stimulated emission depletion (STED) microscopy because they enable super-resolution imaging of the fluorescent proteins which emit in this range, in particular the green and yellow fluorescent proteins (GFP and YFP) and their variants.

Lasers exist which produce yellow-orange light, but each has distinct disadvantages for use in a STED microscope. Titanium:sapphire lasers pumping optical parametric oscillators are used, but are technically complex and often require careful adjustment. Single-color fiber lasers are an option but do not offer valuable spectral tunability. Supercontinuum fiber lasers, due to the fact that they generate broad continua, have low pump conversion efficiencies to narrow wavelength ranges within their output spectrum, ultimately limiting the repetition rate and output power in a narrow spectral range.

This thesis presents a novel light source for STED microscopy based on stimulated Raman scattering (SRS) in standard optical fiber. The source produces pulsed light of high intensity from the green to the red range of the visible spectrum, and can be used to easily attain resolutions of tens of nanometers in a STED image. The physical principles of the SRS light source are discussed. The implementation of three versions with increasing STED imaging performance is demonstrated, with repetition rates increasing from tens of kHz to 20 MHz. With the 20 MHz SRS source beam scanning was incorporated into the STED microscope setup and used for sub-diffraction imaging of living cells expressing GFP- and YFP-fusion proteins.

To date the SRS light source provides the best option for sub-diffraction STED imaging with GFP.

Zusammenfassung. Lichtquellen, die spektrale Flexibilität im gelb-orangen Bereich des sichtbaren Spektrums bieten, sind für die STED-Mikroskopie (engl. *stimulated emission depletion*) von großem Interesse, weil sie beugungsunbegrenzte Abbildungen von fluoreszenten Proteinen, die in diesem Spektralbereich emittieren, insbesondere den grün- und gelb-fluoreszierenden Proteinen (GFP und YFP, vom engl. *green fluorescent proteins* und *yellow fluorescent proteins*) und ihren Varianten, ermöglichen.

Es gibt Laser, die gelb-oranges Licht produzieren, aber diese haben alle ausgeprägte Nachteile für die Benutzung in einem STED-Mikroskop. Titan:Sapphir-Laser, die optische parametrische Verstärker pumpen, werden verwendet, sind aber komplexe Systeme, die oft sorgfältige Justage benötigen. Faserlaser, die nur eine Wellenlänge emittieren, können benutzt werden, bieten aber nicht die wertvolle Spektralflexibilität an. Superkontinuumfaserlaser, die breite Ausgangspektren produzieren, haben eine niedrige Konversionseffizienz vom Pumplicht zum schmalen genutzten Spektralbereich, was schließlich die Repetitionsrate und die Ausgangsleistung in diesem Spektralbereich begrenzt.

Diese Dissertation präsentiert eine neuartige Lichtquelle für die STED-Mikroskopie, die auf stimulierter Raman-Streuung (SRS) in handelsüblichen optischen Fasern basiert. Die Quelle produziert gepulstes Licht mit hoher Intensität vom grünen bis zum roten Spektralbereich des sichtbaren Lichtspektrums und kann auf einfache Weise eingesetzt werden, um eine Auflösung von Dutzenden von Nanometern in einer STED-Aufnahme zu erreichen. Die physikalischen Grundlagen der SRS-Lichtquelle werden erläutert. Der Einsatz von drei Versionen mit steigendem Leistungseigenschaften wird gezeigt, mit steigenden Repetitionsraten von ein paar Dutzend kHz bis 20 MHz. Mit der 20 MHz-SRS-Quelle wird Strahlabtastung implementiert und für beugungsunbegrenzte Aufnahmen von lebenden Zellen, die GFP- und YFP-Fusionsproteine exprimierten.

Derzeit bietet die SRS-Lichtquelle die beste Option für beugungsunbegrenzte STED-Aufnahmen mit GFP.

Contents

1 Introduction

1.1 Far-field Light Microscopy

Far-field optical microscopy is a valuable observational tool because of its ability to non-invasively observe three-dimensional structures within transparent samples. To facilitate its implementation, particularly in the life sciences, structures of interest are often labeled with fluorescent markers. Imaging methods which measure fluorescence photons emitted from such markers enjoy the advantage of high labeling specificity because the markers can be bound to target structures, resulting in the fact that only such structures emit fluorescence light while the rest of the cell remains dark. Excellent signal to noise ratios in fluorescent images result from this high labeling specificity.

Biological samples, however, be they individual cells, tissues, or entire organisms, are complex three-dimensional structures. The spatial features of the structures of interest may be distributed in space in such a way that precludes recording them accurately in all spatial dimensions. As an example, if an image of a cell is made by illuminating the entire cell at once and recording a two-dimensional projection of the fluorescently labeled features within, structures which are separate along the axis of projection will be recorded together in the image, appearing to be localized together though they are not. Thus, *how* the photons are detected is of decisive importance. Both selectively illuminating the sample and determining from where the signal-giving photons originate are important.

The Confocal Microscope

To selectively illuminate the sample, the probing light can be focused by the microscope objective to a single spot, which is scanned through the sample. At each point the signal is recorded, and after scanning an area or volume the signals at each point are assembled to form an image. The focal distribution of light used to excite fluorescence in the sample is called the excitation point spread function (PSF). However, because the light is focused *through* the sample, if fluorescent structures lie above or below the focal spot, they will also be excited and contribute signal, resulting in the registration of signal from different areas of the cell. This is why the method of signal detection becomes important. If a pinhole is placed in the ray path after the lens which focuses the signal onto the detector – properly oriented in space – it overwhelmingly blocks fluorescence light originating from outside the focal spot in the sample. This detection geometry is shown in Fig. 1.1, and forms the basis for the confocal microscope. The detector is only able to see one spot in the sample, called the detection PSF, and is nearly blind to all others. Because background signal originating along the optical axis is blocked, the ability to separate the signal from neighboring structures is increased in all spatial directions, enabling optical sectioning. The spot which is ultimately

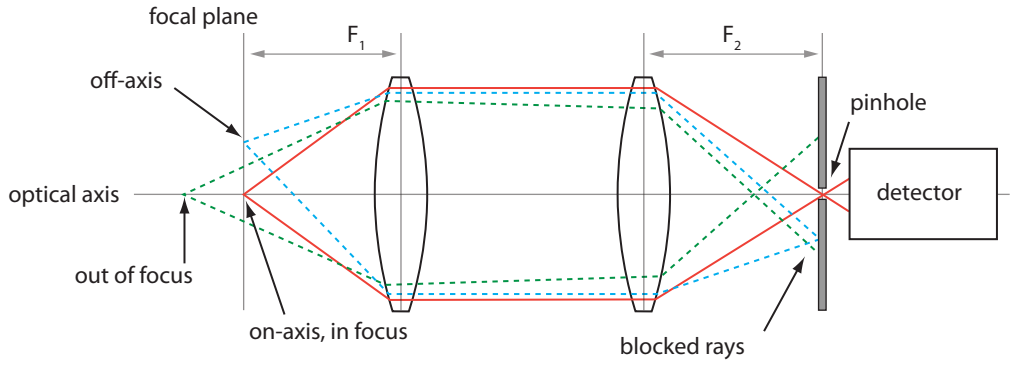

Figure 1.1: Operational principle of the confocal microscope. The placement of a pinhole before the detector overwhelmingly selects photons originating from the focal point, located at the intersection of the focal plane and the optical axis. Photons originating from points not in the focal plane or off the optical axis are blocked by the pinhole. Confocal detection substantially reduces background signal and allows optical sectioning of the sample.

responsible for forming the image is the product of the excitation and detection PSFs, and is called the effective PSF, which is smaller in spatial extent than either by $\sqrt{2}$ [1]. If the detection PSF is decreased to a size much smaller than the excitation PSF, fluorescence light from the periphery of the fluorescence excitation spot is cut out, decreasing the signal, and the resolution does not increase further because it is inherently limited by the excitation PSF.

The Diffraction Limit

With a confocal microscope it is possible to isolate signal originating from small volumes in a sample, but how small are such volumes? Ernst Abbe and later John Strutt (better known as Lord Rayleigh) [2, 3] determined that light is focused by a lens to a finite spot size. The full-width-at-half-maximum of the focal spot in the lateral extent is given by

$$\Delta r \approx \frac{\lambda}{2n \sin \alpha} \tag{1.1}$$

where n is the index of refraction of the medium through which the light is focused and α is the half angle of the focused cone of light, and the quantity $n \sin \alpha$ is called the numerical aperture. A similar formula exists for the extent of the PSF along the optical axis [4]. When yellow light, λ =560 nm, is focused through an objective with a numerical aperture of 1.4, $\Delta r = 200$ nm. This relation for Δr is known as the diffraction limit, is a direct result of the wave nature of light, and is related to the uncertainty principle [5, 6]:

$$\Delta E \Delta t > h. \tag{1.2}$$

If the frequency of the focused light is known, using

$$E = h\nu,$$

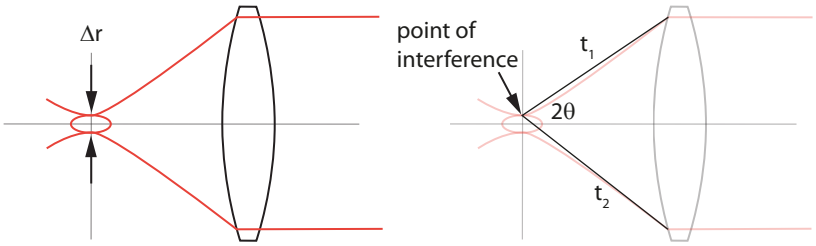

Figure 1.2: The finite width of the focal spot of light focused by a lens due to diffraction. The size of the spot is determined by the relative phases of the photons which interfere at the focus, which is a function of time difference of the two paths shown, t_1 and t_2, which is in turn a function of the half-angle of focusing, θ. This phase difference is related to the uncertainty principle, which can be used with the above relationships to easily approximate Eqn. 1.1.

where h is Planck's constant and ν the frequency of light, leads to the uncertainty in the time taken by two photons taking different paths to the focus

$$\Delta t = t_2 - t_1 > \frac{1}{\nu}. \tag{1.3}$$

This time difference results in the photons having different phases when they arrive at the focus, and the phase relationship gives rise to the intensity distribution at the focal spot. The geometry of the situation is shown in Fig. 1.2. Using Eqn. 1.3, n as the index of refraction of the medium at the focal spot, and solving for Δr, one easily approximates Eqn. 1.1.

To decrease the size of the focal spot the numerical aperture can be increased, but only to an extent. Using two opposing objective lenses, for example, doubles the numerical aperture and is implemented in 4π microscopy [7]. The wavelength of light used can also be decreased, but this is hampered by practical issues such as compatibility with the sample, as many biological structures and fluorescent markers suffer photodamage when exposed to blue or UV light. The restrictions of conventional optical components also become an issue at shorter wavelengths as the transmission of standard glasses decreases in the UV. X-rays induce still more photodamage and are not tractable with conventional optics.

To summerize, the numerical aperture of the imaging system can only be increased so much, and in order to make use of conventional optics and avoid damaging the sample, particularly live cells, the wavelength of light is best kept in the visible region. As a result, practical imaging was limited to using a spot size of ~ 200 nm, limiting the optical resolution to this same magnitude.

Image Formation

The image formed by a microscope is a function of both the object and the imaging system. Every point – here meaning a coordinate with no spatial extent – in the sample which pro-

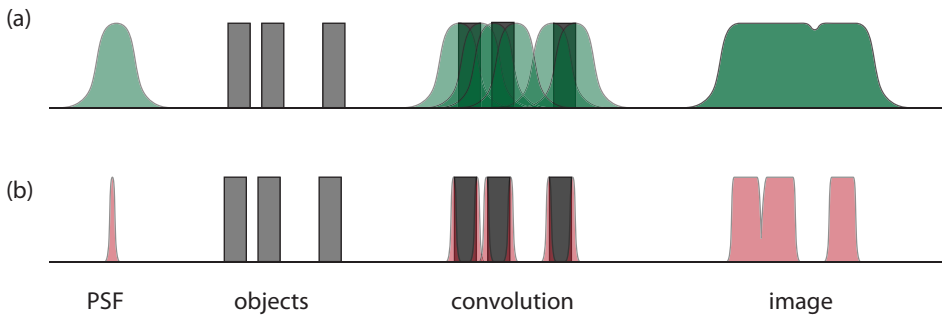

Figure 1.3: The image formation process is shown schematically. The point spread function (PSF) of the imaging system is scanned over the object. Mathematically, this operation is described by the convolution of the PSF and the object, given by Eqn. 1.4. Each point in the object is replaced by the PSF. The process is shown in one dimension for simplicity. All functions are normalized. (a) and (b) show the imaging process with PSFs of different sizes. In (a) details present in the object are lost in the final image, but in (b), with the narrower PSF function, more detail is preserved in the image and it becomes a more accurate representation of the object.

vides signal is recorded by the imaging system not as that point, but the effective PSF. Each signal-giving point is multiplied by the effective PSF, as it is scanned through the sample, to yield the image. This is described mathematically by a convolution,

$$I(x) = (O \otimes R)(x) = \int I(\tau)R(x-\tau)d\tau \tag{1.4}$$

where $I(x)$ is the function describing the resulting image, $O(x)$ is the function describing the object to be imaged, and $R(x)$ is the PSF. Here the convolution is performed in only one spatial coordinate for simplicity. This operation is shown graphically in Fig. 1.4. The spatial extent of the effective PSF which probes the sample limits the resolution of the images which can be obtained. By making $R(x)$ smaller, the object is represented more accurately by the image. This effect becomes noticeable when the scale of the object features is similar to the PSF size. Thus isolated objects which are much smaller in size than the PSF appear to be the size of the PSF in the image, and objects which are separated by a distance similar to the width of the PSF are blurred together and seen as one.

Since a spot of light scanned through the sample is limited by diffraction to $\sim$200 nm, this places a resolution limit on the images obtained. Innumerable cellular structures are smaller than the resolution limit of far-field light microscopy, and as a result remain difficult to observe under physiological conditions. To answer numerous questions in cell biology the true shapes, distributions, and dynamics of biological macromolecules and structures below the diffraction barrier must be seen.

Surpassing the Diffraction Limit Using Light to Switch Molecular States

Simultaneous registration of photons from different markers within a diffraction-limited volume precludes their spatial separation (because the precise origin of the photons cannot be

determined), but if the signals of markers within the diffraction-limited volume can be registered sequentially, the diffraction limit can be overcome. This requires some manner of switching the markers using light within a diffraction-limited volume to their signal-giving states at different times such that their locations can be registered separately. The volume from which the signal originates is effectively reduced below that of the diffraction-limited focal volume. The different states must be distinguished from each other via a measurable quantity. Photons are easily registered, so switching the markers between photon-emitting states and dark states is an attractive ansatz [8, 9]. The fact that the distribution of light on the detector is still dictated by diffraction is immaterial since the photons registered can be assigned to the sub-diffraction volume in the sample from which they originated. Furthermore, standard fluorescent markers can be used, so no change in standard biological sample preparation for imaging is required.

1.2 Fluorescence

Switching markers between a photon-emitting state and a dark state with light can be used to achieve resolution which is not limited by diffraction – but what are the states, and how can the switching be performed? To answer these questions, the properties of the fluorophores used must be understood.

Organic fluorescent molecules possess bound electrons, called π electrons, which are shared between the constituent atoms of the molecules. The energy levels of the π electrons have differences on the order of the energies of photons within the UV, visible, and infrared range of the electromagnetic spectrum. The electronic ground state, S_0, and the first excited electronic state, S_1, are the most important for the current discussion, and are shown in Fig. 1.4 in a Jabłoński diagram.

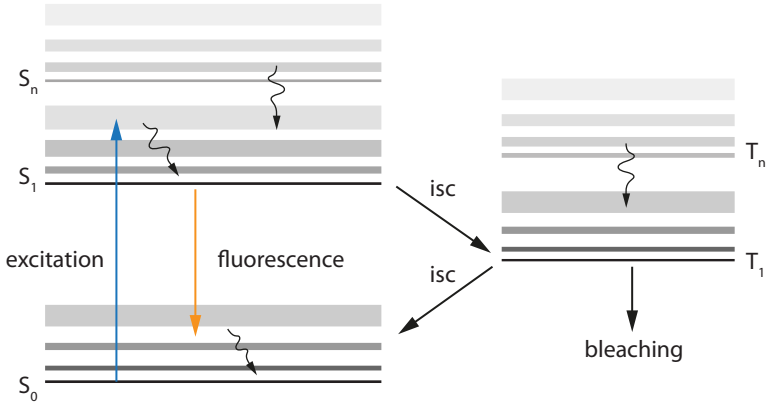

Figure 1.4: Jabłoński diagram of the energy levels of a fluorophore. Singlet states (paired electrons have anti-parallel spin) are denoted by S, and triplet states (spins of electron pairs are parallel) by T. Intersystem crossing, or transitions between singlet and triplet states, is indicated by the arrows labeled *isc*. Relaxation from the higher excited states S_n and T_n back to S_1 and T_1 occurs through vibrational relaxation. Bleaching of the fluorophore occurs primarily via the T_1 and S_1 states.

Photons with energy which correspond to the difference between S_0 and S_1 can excite the fluorophore to S_1. A transition can take place between any thermally accessible vibrational level of the ground or excited states, resulting in a spectrum of photon energies which can excite the fluorophore. This is the excitation spectrum and is shown in Fig. 1.5. The relative amplitude of the spectrum at a given wavelength indicates the relative cross section for photon absorption, σ_{abs}. When in an excited vibrational state of S_1, the fluorophore relaxes to the lowest vibrational state of the energy level within tens of picoseconds. From the vibrational ground state of S_1 it can make the transition to a vibrational state of S_0 with the emission of a fluorescence photon at the rate $k_{\text{fl}} = 1/\tau_{\text{fl}}$, where τ_{fl} is the fluorescence lifetime and is often in the range of 1-4 ns. Due to the spectrum of vibrational levels of the ground state, the energies of the fluorescence photons are also described by a spectrum. The fluorescence emission spectrum is shifted towards the red relative to the absorption spectrum due to the loss of energy to molecular vibration. This spectral shift is called the Stokes shift.

Not all fluorophores excited to S_1 will fluoresce, since there is some degree of vibrational coupling between the S_1 and S_0. This is often influenced by environmental factors such as temperature or the chemical composition of the surrounding media. The probability that the molecule will make a transition to the electronic ground state via the emission of a fluorescence photon is given by the quantum efficiency, which is simply the fraction of fluorophores which do emit a photon from those which are excited.

The states discussed this far are all singlet states, meaning that paired electrons occupying the energy levels have anti-parallel spin. When an electron makes a spin-forbidden transition and flips its spin, so the paired electrons have parallel spin, the excited molecule enters a triplet state, T_n. The excited state T_1 is long-lived, on the order of microseconds, but is usually quenched back to S_0 via interaction with the environment. T_1 presents a major bleaching pathway because it is long-lived and readily reacts with molecular oxygen, destroying the structure and therefore fluorescence ability of the molecule.

1.3 Stimulated Emission

When a fluorophore is in the excited S_1 state it is possible to perturb it with a photon of the proper energy and drive it to the ground state. This is the process of stimulated emission, the phenomenon which forms the basis for operation of the laser [10, 11, 12]. If a photon with energy equal to the difference between the lowest vibrational level of S_1 and a vibrational level of S_0 impinges on the fluorophore, it perturbs the system and drives the fluorophore to the ground state through the emission of an additional photon. Stimulated emission is not only an excellent means for light amplification, but is a convenient mechanism for switching fluorescent media to dark ground states [13, 14, 15, 16, 17].

In principle any fluorophore or fluorescent medium can be switched from the excited fluorescent state to a ground state via stimulated emission. As long as the molecular species has a fluorescence emission spectrum, it also has a cross section for stimulated emission, given by the relation [18]

$$\sigma(\lambda)_{em} = \frac{\lambda^4 E(\lambda)}{8\pi n^2 c\tau} \tag{1.5}$$

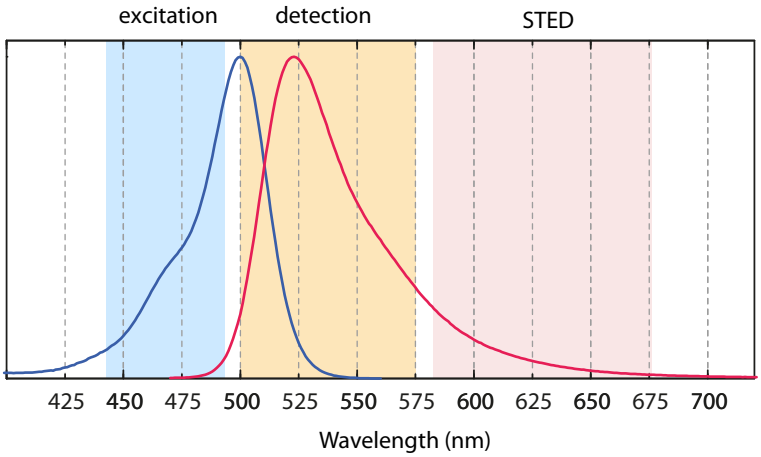

Figure 1.5: Absorption and emission spectra of the Chromeo 488 NHS ester (Chromeon, Tegernheim, Germany) measured in Mowiol, pH 8.4. Spectral regions used for excitation and STED light are indicated, as well as the spectral window used for fluorescence detection. STED light can be applied anywhere in the tail of the fluorescence spectrum where the dye is not re-excited. As the STED light becomes increasingly red-shifted, the cross section for stimulated emission decreases and the efficiency with which the STED beam switches off the fluorescence falls. This functional relationship is given by Eqn. 1.5.

where λ is the wavelength of light, $E(\lambda)$ is the line shape function, giving the probability of fluorescence emission at λ. $\int E(\lambda)d\lambda$ is normalized to the quantum efficiency of the dye. n is the index of refraction of the surrounding medium, c the speed of light, and τ the fluorescent lifetime. However, fluorophores or fluorescent media may also possess non-trivial cross sections for excited-state absorption, σ_{ESA}, limiting the efficiency of stimulated emission as a means to prevent fluorescence [19], though switching to molecular states other than the ground state may achieve the same end.

1.4 STED Microscopy

The first microscopy technique to demonstrate sub-diffraction resolution in the far-field was stimulated emission depletion (STED) microscopy [20, 21]. The approach uses stimulated emission to switch fluorophores at the periphery of the excitation focal spot to the ground state, reducing the volume from which fluorescence photons are emitted and implementing sequential registration of fluorescent markers within diffraction-limited volumes in the sample.

As with conventional fluorescence imaging, the fluorophores are excited with a normal beam of light focused into the sample to form the excitation PSF. This excitation light is accompanied by a second beam of light, spectrally red-shifted from the excitation light. The wavelength of the STED beam is chosen so that it efficiently switches the fluorophores to the ground state S_0 with minimal re-excitation from S_0 to S_1. To achieve this a spectral region is chosen where the absorption cross section σ_{abs} is negligible, but the cross section

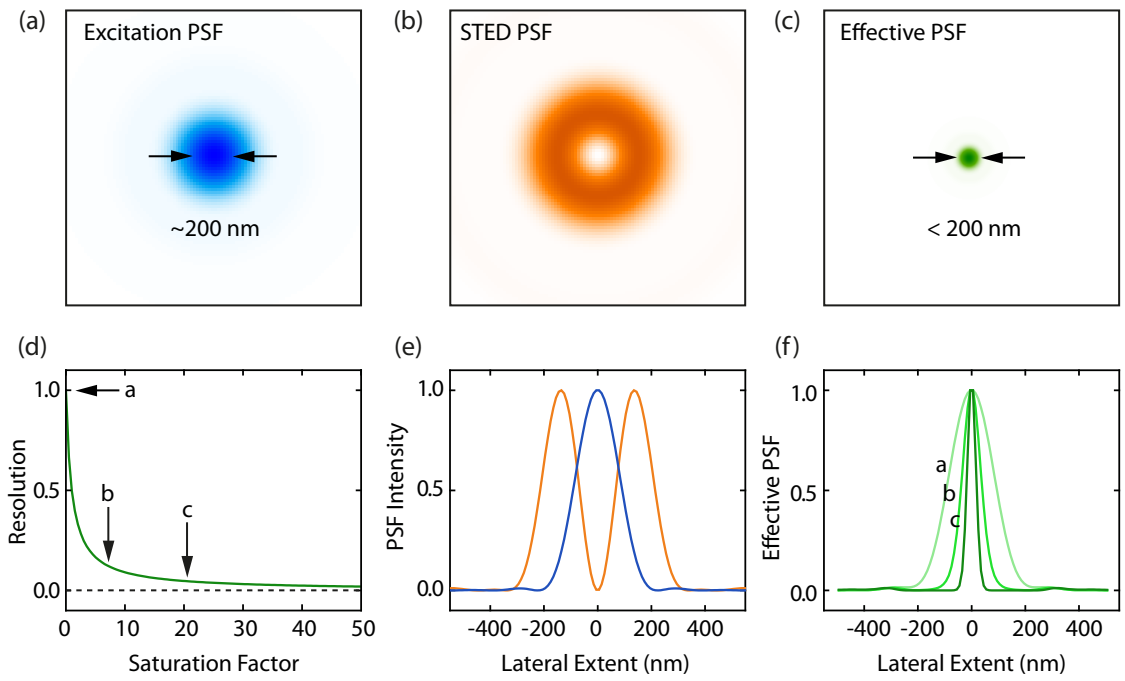

Figure 1.6: The means of STED resolution enhancement. All intensity distributions shown lie in the focal plane. In (a) the excitation point spread function (PSF) and (b) the STED PSF are shown. The superposition of the two PSFs (e) and the switching of the excited fluophores at the periphery of the excitation focal spot back to the ground state result in the decrease in the area of remaining fluorescence, (c), called the effective PSF. The resolution scaling – the scaling of the lateral extent of the effective PSF, (f) – follows the functional dependence shown in (d) and given in Eqn. 1.6. The units of resolution in (d) are given as a fraction of the diffraction-limited resolution, and the saturation factor is the ratio $I_{\mathrm{STED}}^{\mathrm{max}}/I_{\mathrm{sat}}$.

for stimulated emission given in Eqn. 1.5 is large enough. This is shown in Fig. 1.5. The spectral region between the excitation and STED wavelength is used for the detection of the fluorescence signal. The spectral separation of fluorescence and STED light allows the high-intensity STED light to be cleanly separated from the fluorescence signal.

The STED beam is engineered to have a donut-like intensity distribution in the focal plane with a spot of zero intensity in the center, shown in Fig. 1.6. The means of creating the STED donut are shown in Fig. 1.7. As a result, the STED PSF does not switch excited fluorophores at its center to the S_0 state. The excitation and STED PSFs are concentrically aligned in all spatial dimensions so that the spot of maximum fluorescence signal is located at the STED zero, thus yielding the highest fluorescence signal after STED de-excitation.

One crucial fact remains, however. The spatial extent of the STED PSF, with its zero intensity at the center, is also limited by diffraction. How is it then that a sub-diffraction fluorescence volume is obtained by switching states of the fluorophores with these diffraction-limited light distributions? The answer is that the switching is saturable. At a certain intensity of the STED light virtually all of the fluorophores excited to S_1 have been driven to S_0, while those located at the center of the STED PSF, not subjected to STED light, remain in

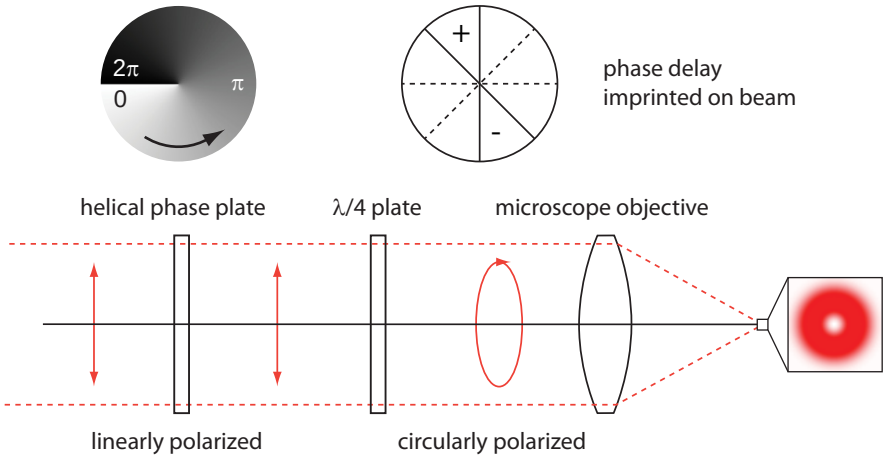

Figure 1.7: Optics used for the creation of the STED donut. The STED beam passes through a helical phase plate, which imprints a ramp-like delay from 0 to 2π into the phase front of the of the STED beam. A phase difference of 2π represents a full period of oscillation for the STED light, so the phase front is sewn together at this location, but portions of the wavefront which pass through opposite sides of the phase plate with respect to the origin have a relative phase delay of π and therefore interfere destructively in the focus of the objective lens. Before being focused the light is circularly polarized, a requirement for proper interference in the focus.

S_1. As the intensity of the STED beam is increased, the volume of fluorophores at the periphery subjected to the STED intensity sufficient to drive them all to S_0 increases, shrinking the volume of those that remain in S_1 at the center. This is shown in Fig. 1.6 (b).

The size of the remaining fluorescent spot, and therefore the resolution of the STED microscope, is a function of the saturation of the stimulated emission transition. The width of the remaining fluorescent volume in the focal plane of the microscope objective is given by

$$\Delta r \approx \frac{\lambda}{2\,\mathrm{NA}\sqrt{1 + I_{\mathrm{STED}}^{\mathrm{max}}/I_{\mathrm{sat}}}} \tag{1.6}$$

with $I_{\mathrm{STED}}^{\mathrm{max}}$ the maximum intensity reached at the crest of the STED donut and I_{sat} the intensity required to switch half the excited fluorophores to the ground state. With a STED intensity of zero the resolution is clearly the same as the diffraction-limited case. The fluorescent spot shrinks with the square root of the STED beam intensity, shown in Fig. 1.6(c). The higher the applied STED intensity, the higher the resolution which can be obtained. Derivations of the formula describing the lateral resolution as a function of STED power are given by [22] and [23].

The ability to saturate the switching from S_1 to S_0 with stimulated emission varies between fluorophores. Re-excitation to S_1 via the absorption of STED photons if the fluorophore has a non-negligible absorption cross section at the STED wavelength, excited-state absorption $S_1 \rightarrow n$, and photodamage can limit the attainable saturation of the transition.

Sub-diffraction resolution can be obtained with STED with both pulsed [21, 24] and continuous wave (CW) lasers [25, 26]. As long as the intensity of the STED light is high enough to saturate the switching of fluorophores from S_1 to S_0 within the fluorescence lifetime, reso-

lution enhancement is obtained. The time-averaged STED power for CW operation is higher, however, since only STED photons which arrive during the S_1 lifetime contribute to the resolution enhancement. The longer the idling periods between excitation pulses during which the fluorophores are in S_0, the higher the average CW STED power must be relative to its pulsed equivalent to obtain the same resolution.

For pulsed STED, the relative timing of the excitation and STED pulses is important. If the STED pulse is placed immediately after the excitation pulse – such that the population of excited fluorophores has attained a maximum and is no longer increasing – and the STED photons fall within the initial part of the fluorescence lifetime, the fluorophores are driven to the ground state before they are able to fluoresce. If the STED pulse arrives later in the fluorescence lifetime, a nontrivial fraction of the fluorophores has already emitted fluorescence photons. If the STED pulse arrives before the excitation pulse, obviously stimulated emission does not occur, since the light falls on molecules in S_0.

2 Motivation

STED microscopy has achieved sub-diffraction resolution on the scale of tens of nanometers in both fixed [24, 27, 28] and living cells [29, 30, 31, 26, 32] and is able to image the dynamics of living biological samples on a variety of time scales, well into the sub-second range. The value of the method for gathering information on the nanoscale within living cells is clear. However, a technical bottleneck to implementing STED is the availability of light sources appropriate for inducing stimulated emission in key spectral regions, in particular in the yellow-orange region of the visible spectrum.

2.1 Simplifying Yellow-Orange Light Sources for STED Microscopy

Tunable light sources which have been used for STED in the yellow-orange region of the visible are often large, expensive, and require careful adjustment or maintenance. Often, to reach the desired wavelength at the proper intensity and pulse length, a number of stages are required.

The traditional work-horse laser is the titanium-sapphire source. The laser medium, titanium-doped sapphire, Ti:Al_2O_3, is itself pumped in the spectral region of 514-532 nm, often with an argon-ion laser or a frequency-doubled Nd:YAG, Nd:YLF, or Nd:YVO laser. Titanium sapphire lasers emit in the range of 650 to 1100 nm, in the red and infrared, so non-linear conversion is required to reach the yellow-orange (550-620 nm) region of the visible spectrum. This can be accomplished with an optical parametric oscillator (OPO), a resonant cavity with a nonlinear crystal [30, 31]. The repetition rate of the Ti:Sa-OPO system is fixed, typically to 40-80 MHz. The pulses are often on the order of hundreds of femtoseconds and must be stretched to hundreds of picoseconds to be suitable for STED (to avoid two-photon absorption or photodamage in the sample), typically with gratings, fibers, or glass rods. Pulse energies are produced in the 550-620 nm spectral range at 80 MHz on the order of 5-15 nJ.

To obtain higher pulse energies – at the expense of lower repetition rates – a Ti:Sa can be used in combination with an optical parametric amplifier (OPA) and regenerative amplifier (RegA) [24, 33]. The OPA also consists of a nonlinear crystal for wavelength conversion, but the crystal is not contained in a resonant cavity. The RegA consists of a resonant cavity with a pumped gain medium. As pulses make many passes through the gain medium the pulse energies are increased substantially, and the amplified pulses are dumped from the cavity. The major disadvantage of this system is the low repetition rates of $\sim$250 kHz, too slow for practical live-cell imaging, despite the complexity of obtaining the desired spectral output.

Fiber lasers are available with yellow-orange output [26], but the output wavelength is fixed, so such systems trade simplicity for spectral flexibility. Supercontinuum fiber lasers,

which produce broad spectral outputs suitable for STED imaging [34, 35, 36], have relatively low spectral conversion efficiencies to specific, narrow wavelength ranges within their output spectrum due to the fact that they generate broad continua. If higher repetition rates or more power is needed within a narrow spectral range, another approach is required.

A simple, spectrally flexible light source, with a high conversion efficiency from the pump wavelength into the yellow-orange region, with pulse energies of several nanojoules and repetition rates of tens of MHz, thus enabling image acquisition speeds sufficient for live-cell imaging, would be of great use for STED microscopy.

2.2 The Importance of GFP

Why is the yellow-orange spectral region of interest for STED? To quote a well-known cell biology text [37]:

> *"GFP tagging is the clearest and most unequivocal way of showing the distribution and dynamics of a protein in a living organism."*

The fact that the ubiquitous green fluorescent protein (GFP), in addition to other fluorescent proteins, emit in the yellow-orange means that they can be used for sub-diffraction imaging with STED only with light sources which produce light of sufficient intensity in this spectral range.

GFP-labeling is well-established in biology and widely used for imaging [38]. Instead of asking biologists to re-design their model organisms to express different fluorescent proteins with emission spectra red-shifted with respect to GFP to be compatible with existing STED lasers sources – at the cost of substantial time and effort – a far better solution is to engineer a simple light source able to yield sub-diffraction-resolution images of the vast number of samples and biological systems which already exist with GFP.

Why not simply use exogenous dyes to label living cells for STED imaging in spectral regions where robust light sources can be used? The answer is that often, labeling target structures within living cells with exogenous fluorescent labels effectively and reproducibly, in such a way that cell function is not altered, is not trivial. The structures of interest must be labeled each time a cell is prepared for measurement. The results are not always deterministic. Fluorophores introduced into the cell which remain unbound contribute to a background signal. In contrast to exogenous labeling, the instructions for fluorescent protein synthesis are encoded in DNA contained within the organism. The fluorescent proteins are bound to target proteins in the cell, resulting in a fusion protein (if GFP is used, a GFP-fusion protein). When expressed by a stable cell line, each cell expresses the fluorescent protein in the same way. Control experiments can be performed on the cell line to ensure that the fusion protein retains the original functionality of the original protein. If the original function of the target protein is provided by the fusion protein, the cell line is relevant for use in further study.

Innumerable model organisms in biology, including pigs, fish, mice, the fruit fly *D. melanogaster*, the nematode *C. elegans*, *E. coli* bacteria, yeast and others have been encoded to express GFP on proteins and structures of interest. To leverage the vast amount of work

required to create these GFP-organism libraries for sub-diffraction imaging, a robust, simple, flexible light source able to perform STED imaging with GFP – in addition to other fluorescent proteins – would be of great value for the scientific community.

3 Stimulated Raman Scattering in Fibers

When high energy laser pulses of nanosecond duration with roughly a microjoule of energy are coupled into standard optical fiber, after several meters of propagation, discrete spectral lines appear, red-shifted relative to the original wavelength. The new wavelengths are generated by stimulated Raman scattering. This simple ansatz is the basis for a light source for STED which fulfills the requirements discussed in the previous section.

3.1 Raman Scattering

In 1928 Chandrasekhara V. Raman described a new scattering process observed when high intensity light was incident upon gases, liquids and optical glass [39, 40]. In addition to the original polarized radiation of photon energy $h\nu_p$, polarized, red-shifted spectral lines were observed with energy $h\nu_s$, where h is Planck's constant and ν is the frequency of the light. Blue-shifted lines were also seen, but far more weakly. Raman recognized that what he observed was a form of inelastic scattering.

At first glance Raman scattering and fluorescence seem similar; both are interactions between light and matter in which energy is absorbed from the incident photons to produce red-shifted radiation. The critical difference is that fluorescence is a resonant process, and Raman scattering is not. The resonance condition anchors absorption and emission spectra within a fixed frequency range. Photons absorbed by the material excite the system to a higher energy eigenstate. For Raman scattering there is no resonance condition and incident

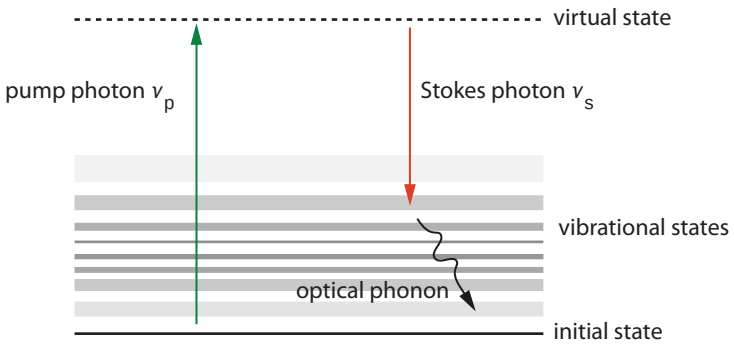

Figure 3.1: Jabłoński energy diagram showing the Raman scattering process.

radiation of any optical frequency can be scattered to produce Stokes or anti-Stokes photons by a fixed frequency shift, $\Omega = \nu_p - \nu_s$. The energy of a scattered photon is not fully absorbed to excite the system to an energy eigenstate, but instead the system is excited to a virtual state. A Jabłoński diagram of the Raman scattering process is shown in Fig. 3.1.

The energy lost or gained by the incident photons is exchanged with optical phonons in the scattering material. If energy is lost, creating Stokes light, optical phonons are created in the scattering medium. If the scattering medium is already in an excited material state and optical phonons are present, the medium can give energy to the scattered light, creating anti-Stokes light. At room temperature anti-Stokes scattering is orders of magnitude weaker than Stokes scattering and difficult to observe.

The Stokes shift is determined by the vibrational modes of the scattering medium, given by the Raman gain spectrum, $g_R(\Omega)$, where Ω is the frequency difference between the incoming and outgoing radiation, $\Omega = \nu_p - \nu_s$. The subscripts p and s distinguish between the pump and Stokes photons. The value of $g_R(\Omega)$ depends on the frequency shift between the incoming photons of energy $h\nu_p$ and the scattered, Stokes shifted photons of energy $h\nu_s$. The maximum value of $g_R(\Omega)$ determines Stokes shift. The Raman gain spectrum for fused silica is shown in Fig. 3.2.

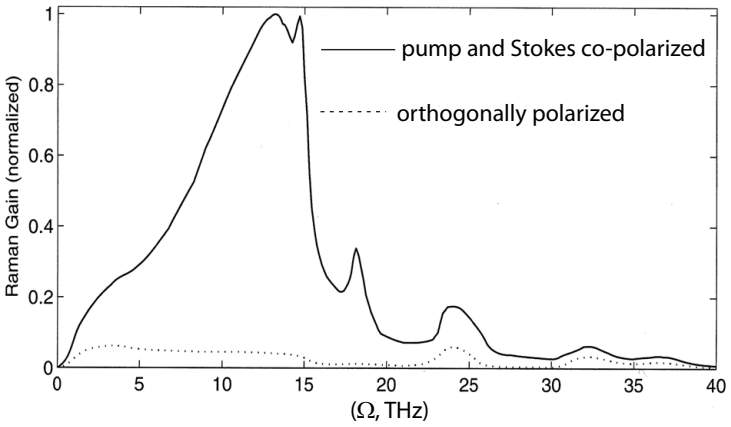

Figure 3.2: Gain spectrum for stimulated Raman scattering (SRS) in fused silica for both perpendicular and parallel polarization orientations of the pump and Stokes light, measured using a pump wavelength of 1 µm, taken from [41, 42].

3.2 Stimulated Raman Scattering

Photons of the proper frequency can stimulate the inelastic Raman scattering process and induce stimulated Raman scattering (SRS), which dramatically increases the intensity of the scattered the Stokes wave,

$$\frac{dI_s}{dz} = g_R I_p I_s \tag{3.1}$$

where g_R is the Raman gain coefficient, characteristic of the scattering medium. I_p is the intensity of the pump radiation and I_s is the intensity of the Stokes radiation. From this relation it is evident that, excluding other effects, the increase in I_s is exponential as the light traverses the scattering material. The relationship between the Raman scattering cross section σ_R and the Raman gain coefficient g_R in cm/W is given by [43, 44]

$$g_R = \frac{\sigma_R \lambda^3}{c^2 h n^2 (N_{ph} + 1)}. \tag{3.2}$$

SRS requires high light intensities because of the small magnitude of g_R, on the order of 10^{-8} or 10^{-9} cm/W for many materials [45] and 10^{-11} cm/W for glasses [44], so it is of little surprise that it was first observed experimentally in 1962 by Woodbury and Ng [46] following the invention of the laser. SRS has since been studied extensively and is a well-known effect [47, 48, 42, 45].

The frequency difference between the photons which induce the stimulated scattering and those of the pump light, $\Omega = \nu_p - \nu_s$, must fall within the gain bandwidth of $g_R(\Omega)$. If the origin of the stimulating photons is spontaneous Raman scattering in the material, this condition is met automatically.

Accurately predicting the Stokes power produced by a given pump intensity is often not trivial due to the numerous additional nonlinear effects which invariably take place in the Raman medium, such as self-focusing, four-wave mixing and stimulated Brillouin scattering [47, 45, 42]. A thorough treatment of SRS is beyond the scope of this thesis. The following discussion is limited to SRS as it occurs within optical fiber as a means for producing light to induce stimulated emission in fluorophores in STED microscopy.

3.3 SRS in Optical Fiber

Despite the small Raman gain coefficient for optical glass, $g_R \approx 10^{-11}$ cm/W, SRS can be prominent within optical fibers at relatively modest powers since high light intensities are maintained over hundreds of meters in the low-loss optical waveguide of the fiber. Efficient spectral generation of Stokes-shifted wavelengths can be achieved. A spectrum created by SRS in a length of optical fiber is shown in Fig. 3.3. A variety of materials have much higher Raman gain coefficients than silica glass, but the challenge to taking advantage of this fact is maintaining high pump intensities over the interaction lengths easily possible in optical fiber.

SRS in optical fibers was observed in 1971 by Stolen, Ippen, and Tynes [44] and is now a well-studied phenomenon [42]. At a threshold optical intensity in the fiber the number of Stokes photons generated by spontaneous Raman scattering becomes large and initiates SRS and the exponential gain in the Stokes wave according to Eqn. 3.1. For fused silica $g_R(\Omega)$ exhibits a maximum of 1.86 $\times 10^{-11}$ cm/W at 13.2 THz for a pump wavelength of 532 nm [49]. The magnitude of $g_R(\Omega)$ varies inversely with the pump wavelength λ_p. For a given pump wavelength, the produced Stokes line is calculated using

$$\lambda_s = \frac{\lambda_p c}{c - \lambda_p \Omega} \tag{3.3}$$

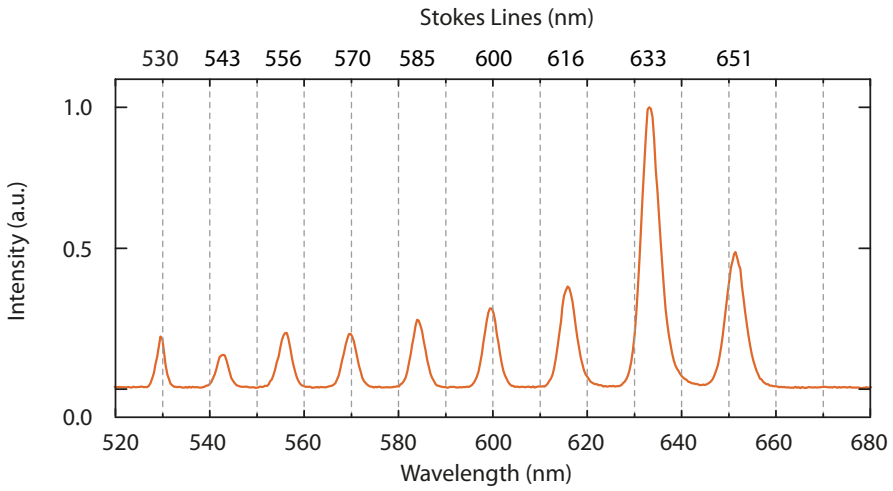

Figure 3.3: SRS spectrum obtained from a 50 m length of Fujikura (Tokyo, Japan) SM63-PS-U40A fiber (with a Ge-doped core). A repetition rate of 1 MHz was used, producing 2 ns pulses, with an average power of 800 mW. Fiber coupling efficiency was 50%.

which is equivalent to

$$\Omega = \nu_p - \nu_s = c(1/\lambda_p - 1/\lambda_s). \tag{3.4}$$

When a Stokes line reaches the threshold intensity, it becomes the pump source for an additional Stokes line. Repeated, this process generates a comb-like spectrum with Stokes lines at regular frequency intervals. Fiber lengths up to the walk-off length (the distance required for pulses of different wavelengths to be separated by dispersion) for the employed pulses increase the gain at the Stokes wavelengths until the effects of power depletion of the pump wavelength or fiber losses at the pump and Stokes wavelengths become appreciable.

Stokes Gain

A quantitative discussion of the Stokes gain follows, considering its chief importance in the creation of the SRS spectrum. Stimulated Raman scattering is a two-photon effect requiring both pump photons to excite the material system and Stokes photons to perturb the system to induce the Raman transition. If only pump photons are present initially, only Raman scattering takes place. Following Hellwarth [50, 48], the photon occupation numbers of the mode fields provide a starting point for a quantitative analysis of the process. The probability per unit time t for the production of a new photon in the Stokes mode via Raman scattering is proportional to the number of photons present in the pump mode, given by

$$\frac{dm_s}{dt} = Dm_p(m_s + 1),$$

where m_p is the mean number of photons per mode in the pump light and m_s is the mean number of photons of the Stokes light. D is a proportionality constant related to the Raman gain and will be determined. The Stokes and pump waves travel at a speed c/n in the z

direction through the scattering medium, where c is the speed of light in vacuum and n is the index of refraction of the material. This gives

$$\frac{dm_s}{dz} = \frac{n}{c}\frac{dm_s}{dt} = \frac{n}{c}Dm_p(m_s + 1). \tag{3.5}$$

In the limiting case when m_s is much smaller than one, $m_s \ll 1$, the physical situation for spontaneous Raman scattering is described, giving

$$\frac{dm_s}{dz} = \frac{n}{c}Dm_p \Rightarrow m_s(z) = \frac{n}{c}Dm_p z.$$

For Raman scattering the Stokes intensity grows linearly with both the length of the medium and the mean occupation number of the pump light mode field. The limit $m_s \gg 1$ in Eqn. 3.5 represents the case of stimulated Raman scattering, leading to

$$\frac{dm_s}{dz} = \frac{n}{c}Dm_p m_s.$$

Defining

$$g_R = \frac{Dnm_p}{c}$$

as the Raman gain coefficient of the material, the expression

$$\frac{dm_s}{dz} = g_R m_p m_s$$

is obtained, leading to the solution

$$m_s(z) = m_s(0)e^{g_R z},$$

showing the exponential growth in the number of photons in the Stokes light over the length of the material. So far the effects of photon losses in the material and depletion of the pump photons have been neglected. The number of photons contained within a given mode is proportional to the optical intensity of the mode, so by making the substitutions $m_p \Rightarrow I_p$ and $m_s \Rightarrow I_s$, the equation

$$\frac{dI_s}{dz} = g_R I_p I_s$$

is obtained. Neglecting photon losses, the total number of photons present is conserved,

$$\frac{d}{dz}\left(I_s + \frac{\omega_s}{\omega_p}I_p\right) = 0.$$

The ratio of the pump and Stokes frequencies arises as a scaling factor to account for the loss of intensity due to the Stokes shift. To account for the losses at both the Stokes and pump wavelengths the absorption coefficients α_s and α_p are introduced, giving the coupled differential equations for the pump and Stokes intensities

$$\frac{dI_s}{dz} = g_R I_p I_s - \alpha_s I_s \tag{3.6}$$

$$\frac{dI_p}{dz} = -\frac{\omega_p}{\omega_s}g_R I_p I_s - \alpha_p I_p. \tag{3.7}$$

With Eqns. 3.6 and 3.7 one can model the evolution of the Stokes and pump powers over the length of the fiber.

Raman Threshold

To solve for the conditions under which the power in the Stokes line becomes equal to the power of the pump line, known as the critical power for achieving the Raman threshold [51], the first term on the right side of Eqn. 3.7 can be dropped, neglecting the depletion of the pump power due to Stokes generation. The solution is substituted into Eqn. 3.6, giving

$$\frac{dI_s}{dz} = g_R I_p(0) I_s e^{(-\alpha_p z)} - \alpha_s I_s.$$

The above equation can be solved, giving the result

$$I_s(L) = I_s(0) e^{g_R I_p(0) L_{\text{eff}} - \alpha_s L},$$

where L is thel fiber length. L_{eff}, the effective fiber length, takes into account the depletion of the of the pump light and is given by

$$L_{\text{eff}} = \frac{1}{\alpha_p}\left[1 - e^{-\alpha_p L}\right].$$

To find the optical power contained within the Stokes wave exiting the fiber, an integral over the frequency range of the Raman gain spectrum is performed

$$P_s(L) = \int \hbar\omega e^{g_R(\omega_p - \omega) I_0 L_{\text{eff}} - \alpha_s L} d\omega.$$

The frequency components near the peak of the gain spectrum are predominantly amplified. With $\omega = \omega_s$, the result obtained by integration is

$$P_s(L) = \hbar\omega_s B_{\text{eff}} e^{g_R(\Omega_R) I_0 L_{\text{eff}} - \alpha_s L}, \tag{3.8}$$

where the effective bandwidth of the Stokes light is

$$B_{\text{eff}} = \left(\frac{2\pi}{I_0 L_{\text{eff}}}\right)^{1/2} \left|\frac{\partial^2 g_R}{\partial \omega^2}\right|_{\omega=\omega_s}^{-1/2}.$$

The Raman threshold is given by

$$P_s(L) = P_p(L) = I_0 A_{\text{eff}} e^{-\alpha_p L}, \tag{3.9}$$

where A_{eff} is the effective core area of the fiber, equal to the mode field diameter of the propagating light. Substituting Eqn. 3.8 into 3.9, assuming a Lorentzian shape for the Raman gain spectrum and making the reasonable approximation that fiber losses at the pump and Stokes wavelengths is the same, $\alpha_p \approx \alpha_s$, the critical pump power obtained is [51]

$$P_{\text{crit}} \approx 16 \frac{A_{\text{eff}}}{L_{\text{eff}} g_R}. \tag{3.10}$$

Using this equation one can predict the critical power, or critical peak power for pulses, at which SRS becomes appreciable in an optical fiber.

Cascading

Once a Stokes line reaches the threshold required for SRS it will become the pump for a further Stokes line. As this process cascades, the characteristic SRS comb spectrum results [52, 53, 54]. The cascading continues until the power contained in the last Stokes line is no longer sufficient to generate the subsequent Stokes line. Modeling the dynamics of the comb spectrum generation and the relative power contained within each Stokes peak involves solving a system of coupled differential equations like Eqns. 3.6 and 3.7, given for the simple case of one pump and one Stokes line.

The power in a Stokes line initially increases over the length of the fiber. When it reaches the critical threshold for the generation of the next Stokes line, its power begins to decrease as power is transferred to the next Stokes line. This process is shown in Fig. 3.4. It is only in the last section of fiber that all the Stokes lines are present. At a fixed fiber length the threshold condition also imposes a maximum power which the pump or any Stokes line can posses. If a line exceeds this power an additional Stokes line is generated and the power of the line is reduced. By tuning the pump power for a fixed fiber length it is possible to maximize the power in a given Stokes line, keeping it below the threshold for the generation of the next Stokes line.

Spectral Broadening

It would not be unreasonable to assume that because the frequency components with the highest Raman gain will experience the most rapid growth, and because this growth is exponential, that each Stokes line would be spectrally narrower than the last in the cascaded SRS spectrum [47]. As can be seen in the spectrum shown in Fig. 3.3 (the FWHM spectral resolution of the spectrometer used for the measurement was 2 nm) and in Fig. 3.5, where the measured linewidth is deconvolved from spectrometer resolution, to approximate of the actual linewidth, this is clearly not the case. Each successive Stokes line is spectrally wider than the last.

The spectral broadening is largely due to the nonlinear phenomenon of self-phase modulation in the fiber [55, 56, 42, 48]. The effect is a result of an intensity-dependent change in the refractive index of the fiber core, given by

$$n(t) = n_0 + n_2 I(t), \tag{3.11}$$

where n_0 is the linear index of refraction and n_2 is the nonlinear-index coefficient. The total index of refraction, as a function of the pulse intensity, changes with time. Different parts of a light pulse experience different values of the refractive index as the they propagate through the fiber – portions of the pulse with higher intensity experience an increase in refractive index – the relative phases of different parts of the pulse are modified as the pulse propagates. These phase shifts give rise to new spectral components and the linewidth of the pulse increases. Nonlinear wave mixing, such as three- and four-wave mixing [42, 48] may also play a role in the spectral broadening of the Stokes lines in SRS [55, 57, 58, 59].

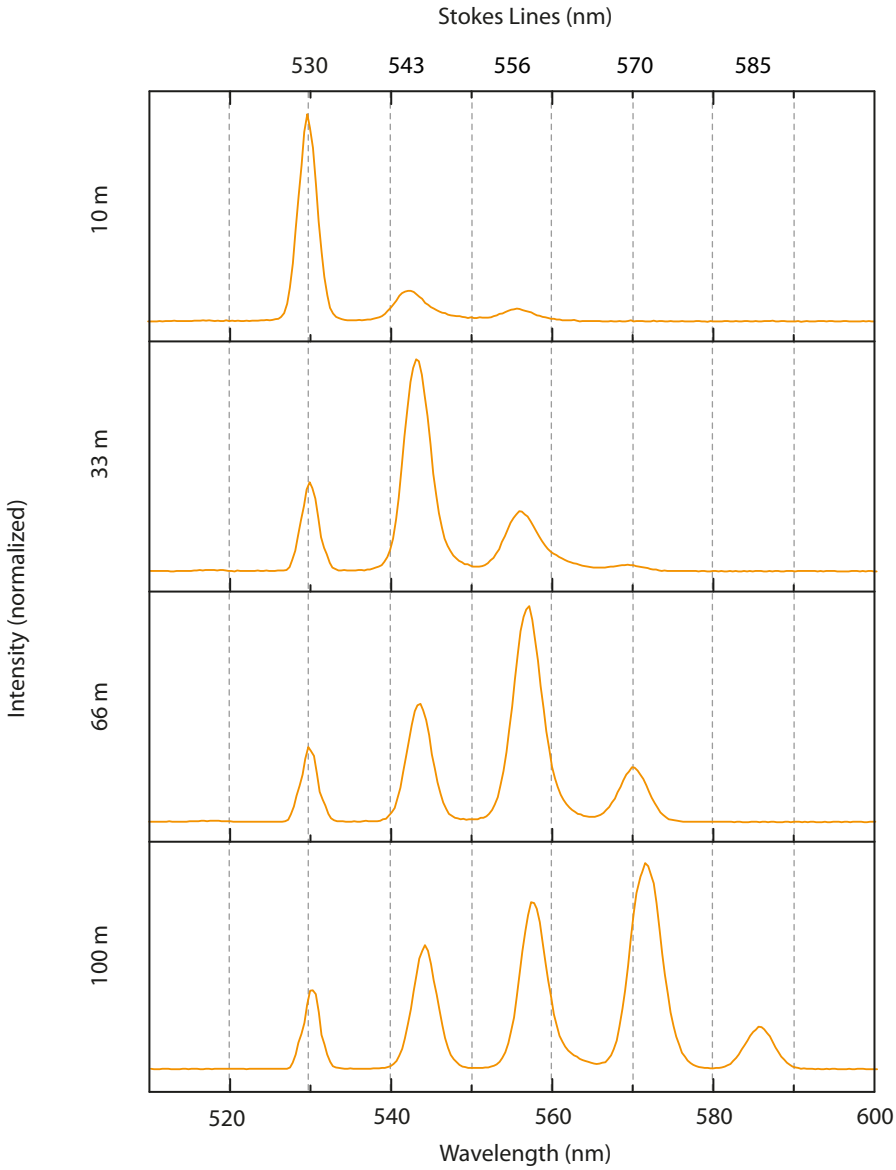

Figure 3.4: SRS spectra as a function of fiber length. The pump pulse repetition rate was 20 MHz with a pulse length of 700 ps and 1.85 W of average power at 530 nm in the fiber (Mobius Photonics, Mountain View, CA, USA). Non-PM Nufern S630-HP pure silica core fiber (East Granby, CT, USA), was used with circularly polarized 532 nm pump light. Maximum light intensities are normalized for a qualitative comparison of spectral structure.

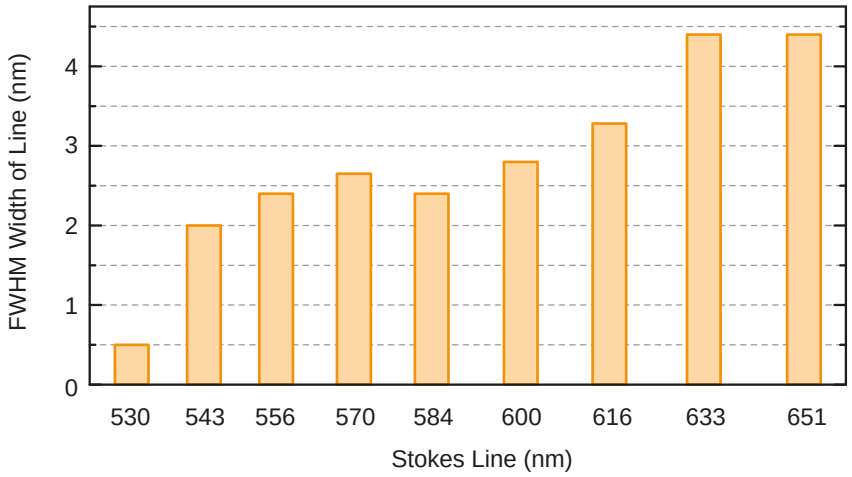

Figure 3.5: The spectral widths of each of the Stokes lines shown in Fig. 3.3. The FWHM resolution of the spectrometer used for the measurement was 2 nm. Assuming Gaussian line profiles, an estimate of the actual FWHM of each Stokes line was obtained. The pump wavelength at 530 nm was specified by the laser manufacturer as having a line width < 0.5 nm.

Dispersion and Pulse Walk-Off

Dispersion within optical fiber must be considered when pulsed light of different wavelengths interact over long lengths of fiber. The group velocity dispersion (GVD) determines the relative speeds at which the different frequencies propagate. For a given pulse length this determines over what length of fiber the two pulses will interact with one another. This distance is called the interaction length, or walk-off length. Clearly the shorter the employed pulses become, the shorter the interaction length for pulses of different center wavelengths. The pulse walk-off limits the efficiency of the cascaded generation of an SRS spectrum, restricting the pulse length of the pump source which can be used effectively [60].

The pulse walk-off length is defined as [42]

$$L_W = \frac{T_0}{\mid d_{12} \mid}, \tag{3.12}$$

where T_0 is the duration of the pulse and d_{12},

$$d_{12} = v_g^{-1}(\lambda_1) - v_g^{-1}(\lambda_2), \tag{3.13}$$

is the walk-off parameter, with v_g being the group velocity. For $\lambda_1 = 500$ nm and $\lambda_2 = 600$ nm, $d_{12} = 3.3 \times 10^{-13}$. This corresponds to a walk-off length of 30 m for a 1 ns pulse. Within this spectral range the approximation can be made that the walk-off length scales inversely with the difference in wavelength.

Temporal Shape of Stokes Lines

The measured temporal shape of the pump and Stokes lines is shown for an SRS spectrum in Fig. 3.6. Dielectric bandpass filters were used to select an individual line for measurement.

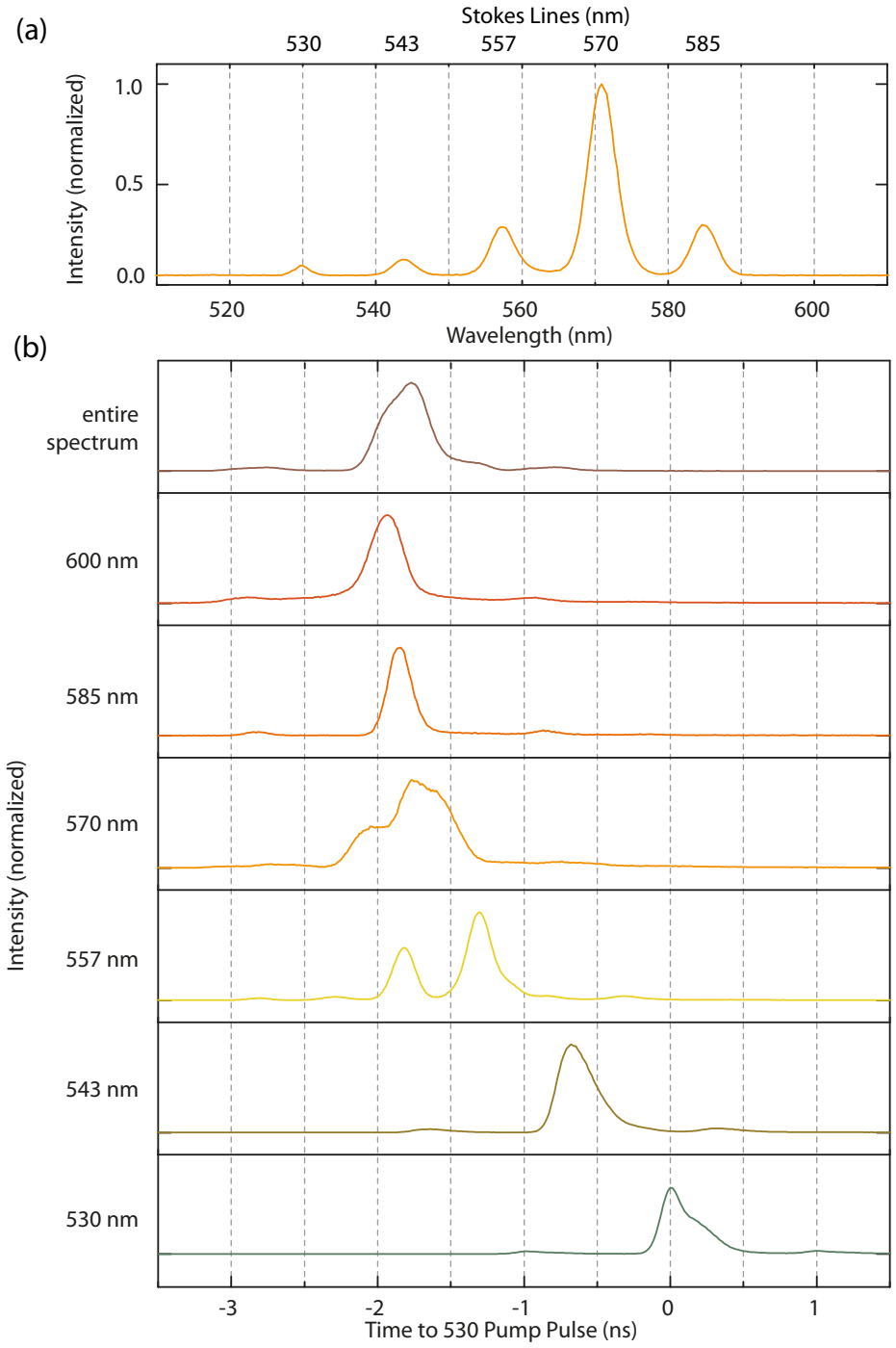

Figure 3.6: (a) SRS spectrum created by a 100 m length of S630-HP Nufern (East Granby, CT, USA) fiber for measurements at 20 MHz used to measure the duration and temporal shape of the Stokes pulses, shown in (b). (b) The pulse lengths and relative pulse timing of SRS light exiting a fiber. The individual Stokes lines (indicated to the left of the data) were spectrally separated by the use of dielectric band-pass filters. Photons were registered with an avalanche photodiode (id Quantique, Geneva, Switzerland) in combination with a time-correlated single photon counting measurement board (Becker and Hickl, Berlin, Germany). The signal from a fast photodiode registering pump pulses from the laser was used as the trigger for the measurement. The top pane of (b) shows the temporal shape of the entire SRS spectrum exiting the fiber. Because of the large variation in the relative intensities of the each Stokes line, only the most intense features are evident in this temporal profile. The light in the last Stokes line, at 600 nm, is too dim relative to the other Stoke line to be seen in (a).

Photons were registered with an avalanche photodiode (id Quantique, Geneva, Switzerland) in combination with a time-correlated single photon counting measurement board (Becker and Hickl, Berlin, Germany). The pulse shapes are determined by several processes which take place simultaneously in the fiber. A pulse has a range of frequency components and the temporal length of the pulse will increase as the different frequency components travel in the fiber at different speeds as a result of GVD. Additionally, the intensity peak of the pulse will experience a delay due to the nonlinear index change of self-phase modulation [56].

Both of these effects are independent of the cascaded generation of the Stokes lines. As the peak intensity of a spectral line reaches the threshold for the generation of a Stokes line, power is initially transferred from the peak of the pump pulse to form the Stokes line. Being red-shifted from its pump pulse, the Stokes pulse travels faster and walks off the front of the pump pulse, depleting the intensity of the pump as it sweeps forward as both propagate along the fiber.

Thus the shape of a given pulse is a function of its intensity, the distance it has propagated in the fiber, and the exchange in power between it, its pump pulse, and its Stokes pulse.

Polarization

SRS is a polarization-dependent effect. This fact can be clearly seen from the difference between the Raman gain spectra for co-polarized and orthogonally polarized pump and Stokes light. As a consequence, attention must be paid to the polarization state of the light in the fiber during SRS. For stable spectral generation the pump and Stokes lines can be co-polarized in a polarization-maintaining (PM) fiber, or both circularly polarized in a non-PM fiber. The Raman threshold, given by Eqn. 3.10 for the circularly polarized case is twice that of the linearly polarized case [42].

The situation to be avoided is where the polarization states of the pump and Raman lines are not maintained, as the case when linearly polarized pump light is coupled into a non-PM fiber. Small perturbations then flip the polarization state of the light in the fiber, resulting in large fluctuations in the efficiency of SRS and hence large fluctuations in the power of the Stokes lines.

Material Composition

The material composition of the fiber core is important as it determines the magnitude of the Raman gain coefficient [61, 62, 63, 64, 65, 66], the frequency shift of the Stokes wave due to the structure of the gain spectrum and the propensity of the fiber to be damaged by photodarkening when transmitting high optical intensities.

Fused SiO_2 forms the material basis for most fibers and dopants are often added to both the core and the cladding to achieve the necessary index mismatch. For example, the dopants GeO_2 and P_2O_5 increase the refractive index of SiO_2 and are added to the core, while boron and fluorine decrease the refractive index of silica and are used in the cladding [42]. Active fibers, used for fiber amplifiers or fiber lasers, are doped with rare earth ions. The values of the Raman gain coefficient, g_R, for several glass types are given in Table 3.1. Also listed is

the frequency shift for the gain peak(s) and the pump wavelength used for the measurement. Values are obtained from [49] and [61] with use of Eqn. 3.2.

Table 3.1: g_R for different glasses, calculated using the g_R value for silica given by [49], Eqn. 3.2, and relative Raman cross sections given by [61]. * P_2O_5 exhibits two peaks.

Glass Type	$g_R \times 10^{-11}$ (cm/W)	Pump Wavelength (nm)	Peak Frequency Shift (THz)
SiO_2	1.86	532	13.2
GeO_2	14	514.5	12.6
B_2O_3	8.5	514.5	12.2
P_2O_5 *	9.4	514.5	19.2
P_2O_5 *	5.8	514.5	41.7

4 Experiments

Experiments using SRS to generate light to be used for de-excitation in STED microscopy were performed in three stages of technical implementation: First a compact, relatively cheap 532 nm, diode-pumped, frequency-doubled solid state laser source with a 60 kHz repetition rate was used to demonstrate the viability of the concept. Though the initial results were promising, system performance was severely limited by the low pump repetition rate, which led to long image acquisition times.

To implement the SRS light source with a higher repetition rate, a different pump laser architecture was subsequently employed: a master-oscillator, power amplifier (MOPA) system capable of a 1 MHz repetition rate while providing requisite pulse energies and similar pulse lengths. Improved image quality and reduced image acquisition time were demonstrated. An advantage of the MOPA laser architecture is that system parameters such as repetition rate and pulse length can be changed electronically.

For the last stage of measurements the repetition rate of the MOPA pump source was increased to 20 MHz, bringing image acquisition times into a regime which enabled the implementation of a beam-scanning setup. Live-cell STED imaging with fluorescent proteins, variants of the green and yellow fluorescent proteins, was performed.

4.1 kHz Dioded-Pumped, Solid-State Laser Pump Source

Initially a diode-pumped solid state (DPSS) frequency-doubled microchip laser was used as a pump source, operating with an output repetition rate of 60 kHz, and providing 30 mW of average power with 1 ns pulses. The average pulse energy was 0.5 µJ and the spectral linewidth 0.3 nm (Alphalas GmbH, Göttingen, Germany). A relatively stable comb spectrum was generated starting from the pump wavelength at 532 nm to 620 nm, shown in Fig. 4.2. Due to large pulse energy fluctuations – the pulse energies were bimodally distributed with approximately half the pulses containing twice the energy of the remaining half – the repetition rate fell for each Stokes line, as shown in Fig. 4.3. The final Stokes line used for STED measurements, at 620 nm, had a repetition rate of roughly 18 kHz.

Fig. 4.1 provides a schematic of the setup used. 532 nm green pump light exited the DPSS microchip laser and was separated from the 1064 nm fundamental light remaining in the laser output beam with a colored glass filter. Polarization optics, a Glan-laser prism and a half-wave plate, were placed in the beam path to control the laser power to be coupled into the fiber and to turn the polarization orientation to coincide with one of the birefringence axes of the polarization maintaining fiber in which the SRS light generation took place. A simple lens was used to couple the pump light into the fiber.

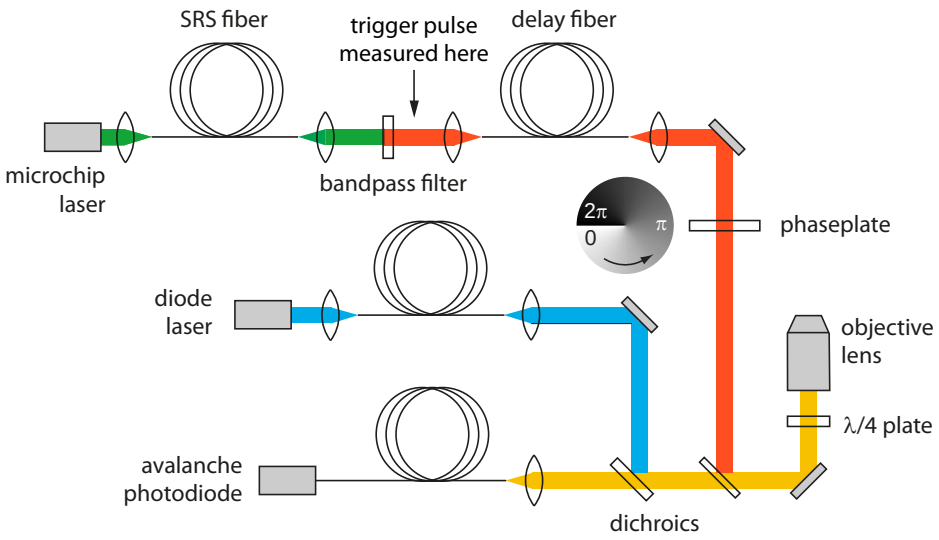

Figure 4.1: Setup used for STED measurements using the 532 nm, kHz DPSS microchip laser pump source. The delay fiber was needed because of the energy fluctuations in pulses of the pump source, which caused different Stokes lines to have different repetition rates. The pulses from each Stokes line to be used as STED light needed to be synchronized to the excitation diode laser, requiring the delay fiber.

Light exiting the fiber was collimated and the desired Stokes line to be used for STED light was selected with a dielectric band pass filter. A small fraction of the STED light was directed to a fast photodiode for the purpose of triggering the excitation laser diode, a requirement due both to the pulse-to-pulse temporal jitter and the pump light intensity fluctuations which resulted in a different repetition rate for each SRS spectral line. For this second reason the fast photodiode was not placed before the SRS fiber; if the excitation pulse was triggered via a 532 nm pump pulse which did not contain sufficient intensity to generate the used STED wavelength, an excitation pulse without the corresponding STED pulse would be triggered. To provide the electronics for the excitation source time to respond to the trigger input, a second fiber, 30 m in length, was included to provide an optical delay for the STED pulse. Light from this fiber was collimated and directed through a helical phase delay plate (RPC Photonics, Rochester, NY, USA) and reflected by a dichroic mirror through a quarter waveplate into an 100×, oil immersion 1.4 NA UPlanSApo apochromatic microscope objective (Olympus, Tokyo, Japan), where the combination of both the helical phase imprint on the wavefront and the circular polarization of the STED light created the donut STED light distribution in the focal plane.

Two diode lasers were employed as excitation sources depending on the fluorophores used for imaging; either a 440 nm source providing 130 ps pulses or a 470 nm source with 70 ps pulses (PicoQuant, Berlin, Germany). Excitation light was coupled into a short length of fiber to spatially clean the beam profile, and the collimated excitation light was directed to the objective via a second dichroic mirror. The fast photodiode, triggered by the STED pulse, in combination with delay cables and an electronic delay box, ensured that the excitation and

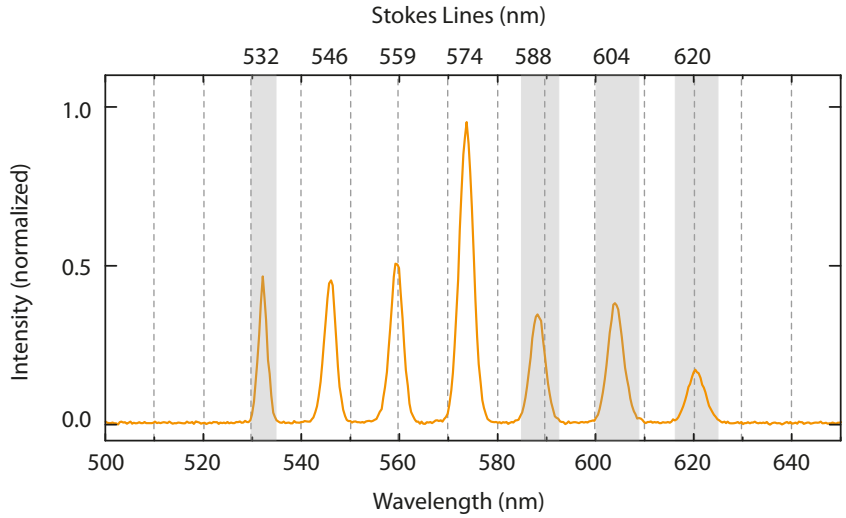

Figure 4.2: Spectrum used as a source of STED light for kHz SRS STED imaging experiments. The lines used as STED light for measurements are indicated with gray bars. A PM Fujikura fiber (Tokyo, Japan) with a 4 µm core diameter and a GeO_2:SiO_2 core composition with a 410 nm cut-off wavelength was pumped with 1 ns, 532 nm pulses, with energies of 100-250 nJ in the fiber.

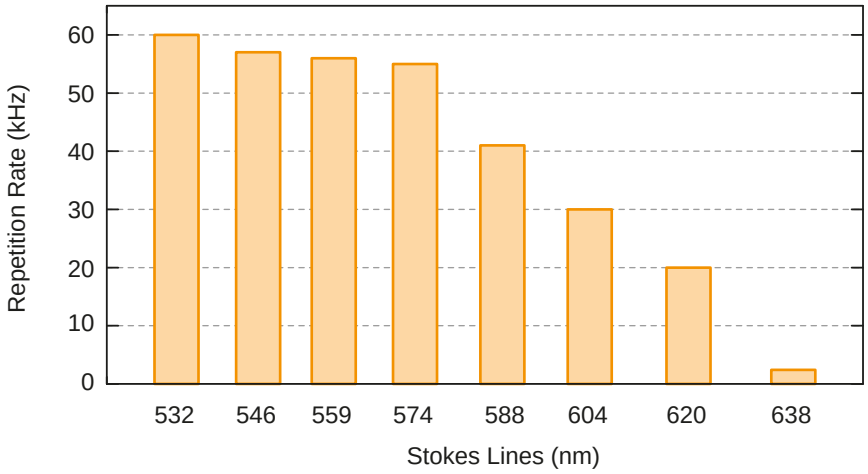

Figure 4.3: Repetition rates of the Stokes lines generated in the fiber pumped by the 532 nm DPSS microchip laser. The repetition rate falls with each Stokes line as a consequence of the large pulse energy fluctuations of the pump source.

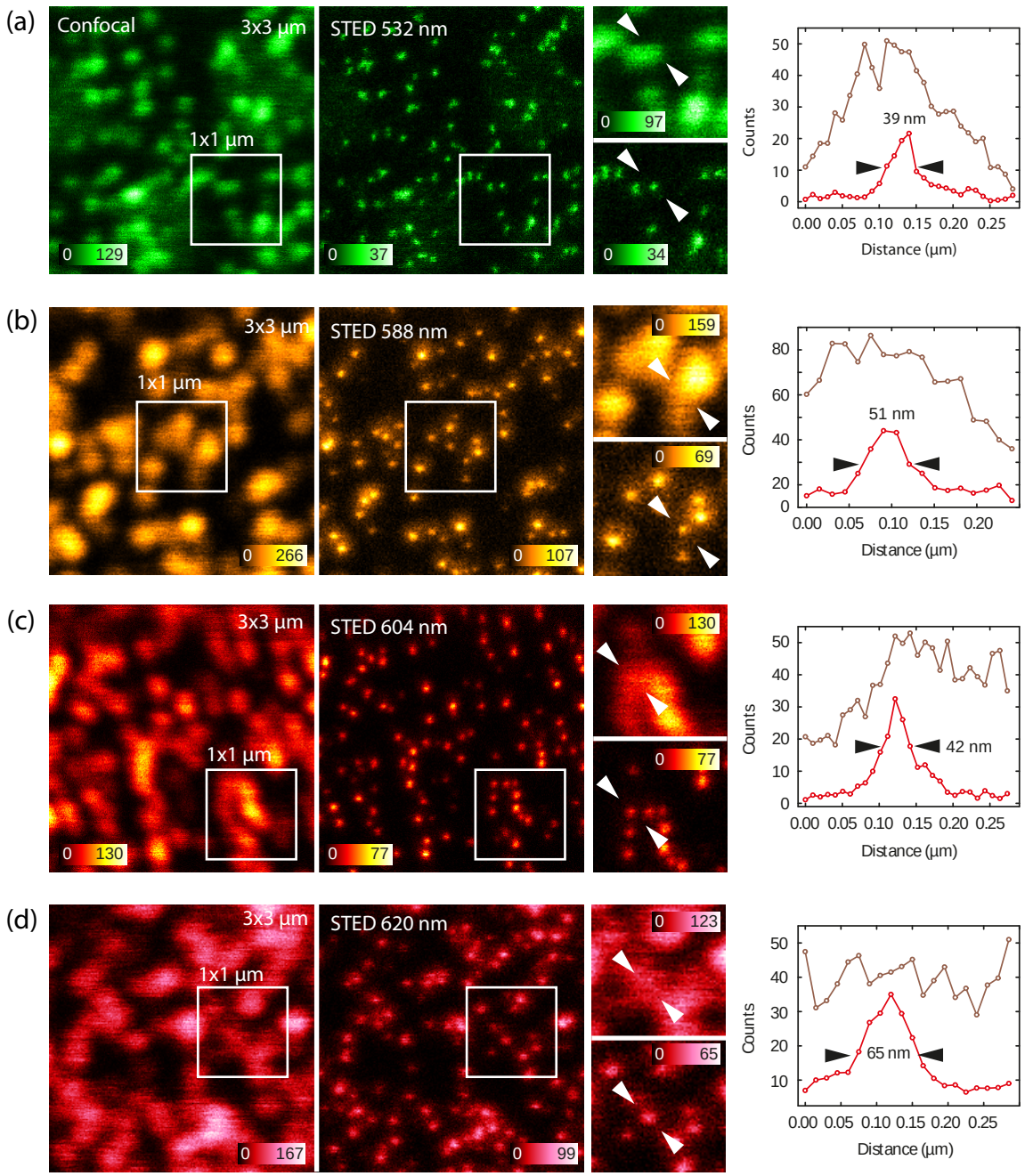

Figure 4.4: STED images of fluorescent nanospheres taken with the kHz SRS STED source, with standard confocal images at left for comparison. Large images are 3x3 µm, small insets are 1x1µm, and line profiles are taken at locations indicated by arrows. (a) STED using the 532 nm pump wavelength as de-excitation light to obtain images of silica nanospheres labeled with Atto 425. 440 nm excitation light was used. (b) STED images obtained with the 588 nm, (c) 604 nm, and (d) 620 nm Stokes lines as de-excitation light, in each case using yellow-green fluorescent nanospheres (Invitrogen, Carlsbad, USA) as samples. In (b), (c), and (d) 470 nm excitation light was used. All data shown is raw, and each pane shows the full dynamic range of the image.

STED pulses reached the sample simultaneously.

Fluorescence photons emitted by the sample were gathered by the objective lens, directed through the dichroic mirrors and focused into a multimode fiber, which acted as the confocal pinhole, and brought to an avalanche photodiode (Perkin Elmer, Vaudreuil, Canada) for registration. The sample was scanned over the objective lens through the stationary focus to form the image with a piezo stage (Melles Griot, Albuquerque, USA). The information from the detected photons at a given stage position was used to construct an image using Imspector, an imaging software package developed in-house.

A length of polarization-maintaining fiber 50 m long was used which had a nominal cut-off wavelength of 410 nm and a 4 μm core diameter (Fujikura, Tokyo, Japan). The core of the fiber was specified by the manufacturer as being Ge:O_2 doped. A fiber coupling efficiency of 50% was achieved, providing optical intensities of 500 MW/cm^2 at 532 nm in the fiber core, generating six Stokes lines, out to 620 nm. The light of each Stokes line was polarized exiting the fiber.

Substantial pulse-to-pulse temporal jitter on the order of 1 μs required the excitation sources, 440 nm and 470 nm pulsed diode lasers (PicoQuant, Berlin, Germany), to be synchronized to the STED output in a pulse-by-pulse fashion using the signal from a fast photodiode after the SRS fiber to electronically trigger the excitation pulses. The choice of excitation wavelength depended on the fluorophore used, and the wavelength which provided more efficient excitation was employed.

As a result of the slow repetition rates, image acquisition times were long, typically 10 to 20 minutes for a 2×2 μm image. Pixel sizes of 10 to 20 nanometers were used with pixel dwell times of 15 to 30 ms. Images were first made using the output of the pump source at 532 nm, shown in Fig. 4.4 (a). Self-made silica beads containing Atto 425 (Atto Tec, Siegen, Germany) 20 to 30 nm in size were imaged. Photobleaching was prominent, however, and was minimized by treating the samples with DABCO (1,4-Diazabicyclo[2.2.2]octan) (Roth, Karlsruhe, Germany). To demonstrate STED imaging with the light generated via SRS, the last three Stokes lines, at 588, 604, and 620 nm were used. Images are shown in Fig. 4.4 (b)-(d). For these wavelengths yellow-green fluorescent beads (Invitrogen, Carlsbad, USA) with two different average sizes of 24 and 43 nm in diameter, specified by the manufacturer, were used as samples. FWHM measurements of the bead diameters in STED images yielded values of 70-80 nm averaged over x, y, and both diagonal directions. Using the knowledge of the bead size and the FWHM measurement of the bead images in STED images, effective point-spread functions of 58 nm (for STED at 588 and 604 nm) and 78 nm (for STED at 620 nm) were calculated.

Photodarkening was observed in the fiber used for the kHz-source experiments. Initially 8 Stokes lines were observed in the SRS spectrum extending to 656 nm, but in the first hours of operation with the new fiber the generation of the last two lines ceased. A concomitant reduction in fiber transmission was also observed. After this initial change, however, the fiber properties were stable for ∼6 months. After this time, however, the output polarization of the fiber became unstable. The polarization direction of the output light would hop between the birefringent axes with an irregular periodicity, indicating damage to the birefringent properties of the fiber. This observed polarization instability ultimately limited the lifetime of the fiber.

Despite these difficulties, however, the compact, simple light source provided a proof-of-principle of the approach to use SRS in standard fiber for STED microscopy.

4.2 1 MHz Master Oscillator, Power Amplified Fiber Laser Pump Source

Image acquisition with a STED source operating at a repetition rate in the tens of kilohertz is extremely slow and impractical for normal imaging applications. To push the concept of using SRS to generate STED light further, a pump laser with similar pulse energies but a higher repetition rate was required, necessitating a change in pump laser architecture. The source employed for this improvement was a fiber laser based upon a master-oscillator, power-amplifier (MOPA) architecture (Mobius Photonics, Mountain View, CA, USA) [67, 68]. The pulse length and repetition rate of the system were determined by the master oscillator, a low-power laser diode. The light was then fiber-amplified in multiple stages to reach suitably high power levels before the amplified 1060 nm output was frequency doubled to provide 530 nm. 2 ns pulses were used with an available pulse energy of 10 µJ, as 10 W of average power were produced at the output. Only a fraction of this total power was required to obtain the Stokes lines of interest for STED experiments. The spectral bandwidth at 530 nm was < 0.5 nm.

Additional improvements over the DPSS source included much reduced temporal pulse jitter, on the order of 1 ns (still necessitating triggering the excitation laser from the STED pulse) and much reduced pulse-to-pulse energy fluctuations ($3\sigma < 10\%$, where σ is the standard deviation of the pulse energy distribution), eliminating the fall in repetition rate with each red-shifted Stokes line.

The microscope setup employed to demonstrate the imaging capability of the 1 MHz source was similar to that described in the previous section for the kilohertz pump source. The setup used is shown in Fig. 4.5. The delay fiber after the SRS fiber was eliminated and the placement of the fast photodiode for triggering the excitation source synchronously with the STED light was moved to directly measure the 530 nm pump pulses before the SRS fiber. This simplification was possible because of the reduced pulse energy fluctuations resulting in the same repetition rate for all STED lines. The only reason to trigger the excitation from the pump pulses was to counter the effects of the $\sim$1 ns temporal pulse jitter.

A 20$\times$ microscope objective (Olympus, Tokyo, Japan) was used for focusing the pump light into the fiber, and a piezo stage was used to position the fiber at the focus of the objective lens. Using the piezo stage reduced the time required to couple the fiber and permitted the user to optimize the coupling remotely and accurately during high-power operation.

Polarization maintaining fiber with a mode field diameter of 4.1µm at 630 nm and a nominal cut-off wavelength of 530 nm was used (Fujikura, Tokyo, Japan). The fiber used for measurements was 100 m long. The fiber core was doped with Ge:O_2, as specified by the manufacturer, but at undisclosed concentrations. Reductions in fiber transmission were observed during the initial use of the fiber. Including coupling losses initially 50% of the launched light was transmitted, but this value soon fell to 20%, resulting in optical intensities of 50 MW/cm^2 of the pump light in the fiber core. The walk-off length for neighboring Stokes lines for 2 ns pulses was greater than 100 m.

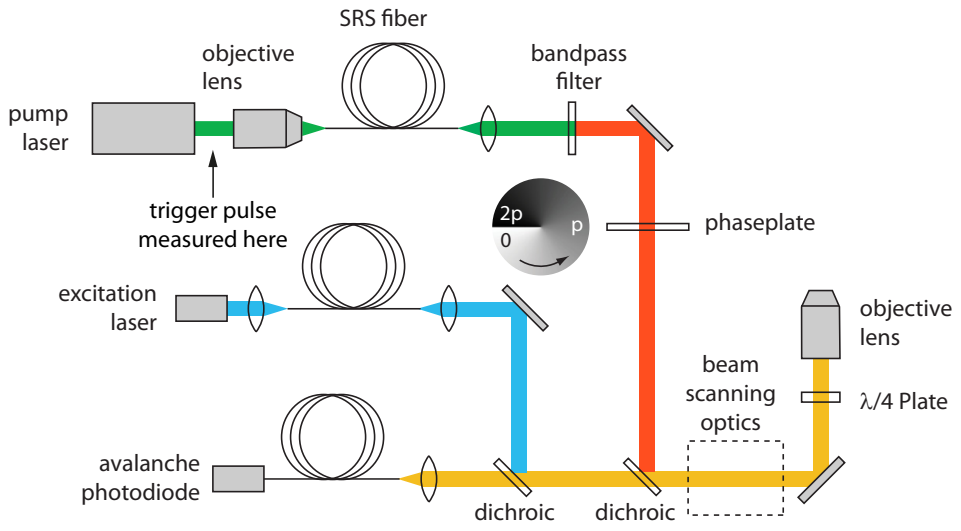

Figure 4.5: Setup used for STED measurements with both the 1 and 20 MHz pump source. Because of the negligible energy fluctuations present in the pump source, no delay fiber is needed between the SRS fiber and the objective lens. The location of the beam scanning optics, shown in Fig. 4.10, for the 20 MHz measurements, is indicated.

Of additional note is that the power contained within a given Stokes line was tunable due to the cascaded nature of the spectral generation. By changing the 530 nm pump power, one could extend or reduce the spectral extent of the SRS spectrum, as shown in Fig. 4.6. At the proper pump power, the last Stokes line was the most intense, just as the power contained within the last peak became saturated (*i.e.* before the creation of an additional Stokes line). Thus, by tuning the pump power, power could be efficiently placed in the Stokes line where it was needed.

STED images using the last three lines at 585 nm, 600 nm, and 616 nm were obtained with both yellow-green fluorescent nanospheres (Invitrogen, Carlsbad, USA) and vimentin fibers, constituents of the cytoskeleton, in PtK2 cells labeled with Chromeo 488 (Chromeon, Tegernheim, Germany), via secondary antibody labeling. Data are shown in Figs. 4.7 and 4.8. STED pulse energies in the back aperture of the objective lens varied between 2 and 8 nJ depending on the wavelength used (higher STED were typically used for redder depletion wavelengths, as the cross section for stimulated emission becomes smaller while using the same fluorophore). Pixel sizes of 10 nm were used for bead samples while 20 nm pixels were used to obtain STED images in biological samples. Pixel dwell times varied from 0.5 to 1 ms. Acquisition time for an image 4×4 µm in size with a 0.5 ms pixel dwell time and pixels 10 nm in size equated to approximately 6 minutes.

The STED resolution obtained in bead images was obtained using an in-house written image analysis program to superimpose the individual bead images contained in a single STED recording, align their centers, and add their signals, performing a Gaussian fit in the x,

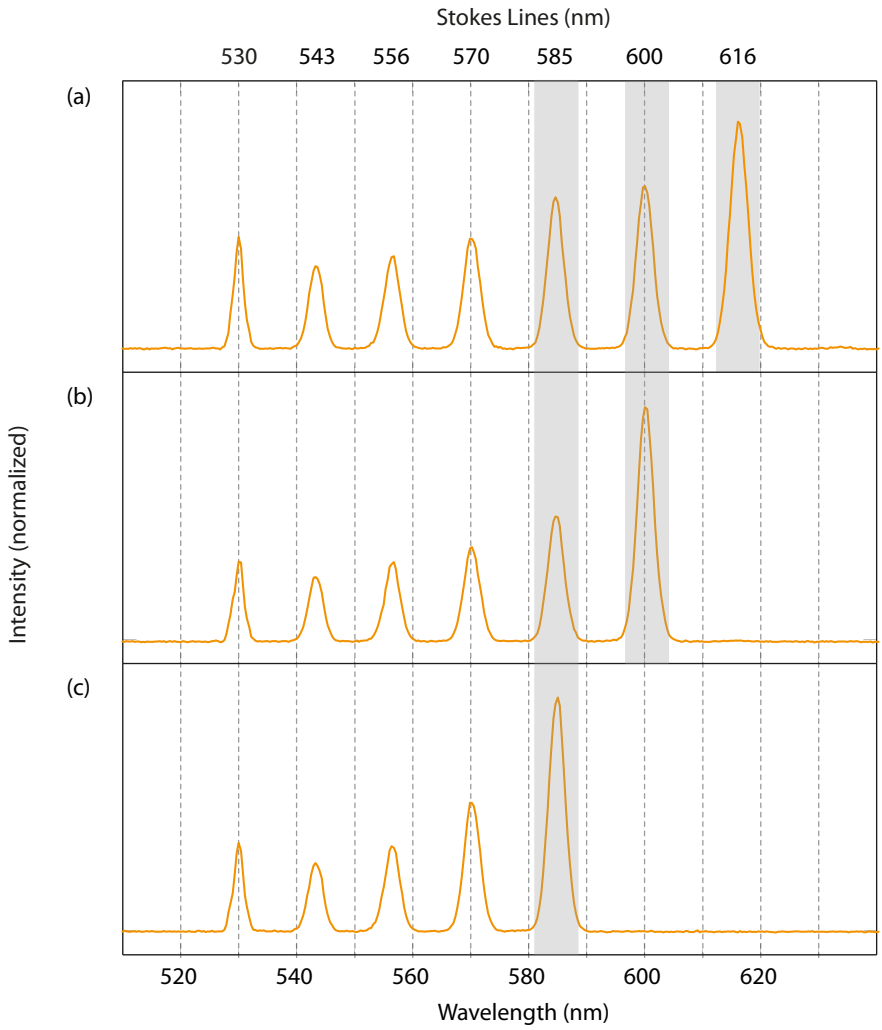

Figure 4.6: SRS spectra used to generate (a) 615 nm, (b) 600 nm, and (c) 585 nm STED light at 1 MHz, indicated with gray bars. The 530 nm powers used in each case, before coupling into the fiber, were (a) 360 nm, (b) 240 mW, and (c) 200 mW. The cascaded nature of the SRS spectrum generation was used to maximize the power in the last Stokes line in each case.

y, and diagonal orientations in the summed image. 90 or more individual beads were sampled from a single STED image, excluding those too close to their neighbors to be resolved or fitted, or beads which appeared to be present in agglomerations. The manufacturer specified the beads as having a diameter of 43$\pm$6 nm. A FWHM value of the effective point spread function of 20 to 30 nm was obtained by approximating the object function, the effective point spread function, and the image function as Gaussians and performing a deconvolution.

To determine the resolution obtained in images of vimentin fibers in PtK2 cells, multiple FWHM intensity line profiles were taken perpendicular to the fiber direction. Values of 60 to 100 nm were obtained. Based upon the knowledge that the actual vimentin fiber diameter together with secondary antibody labeling of the fluorophores was $\sim$50 nm, and again making

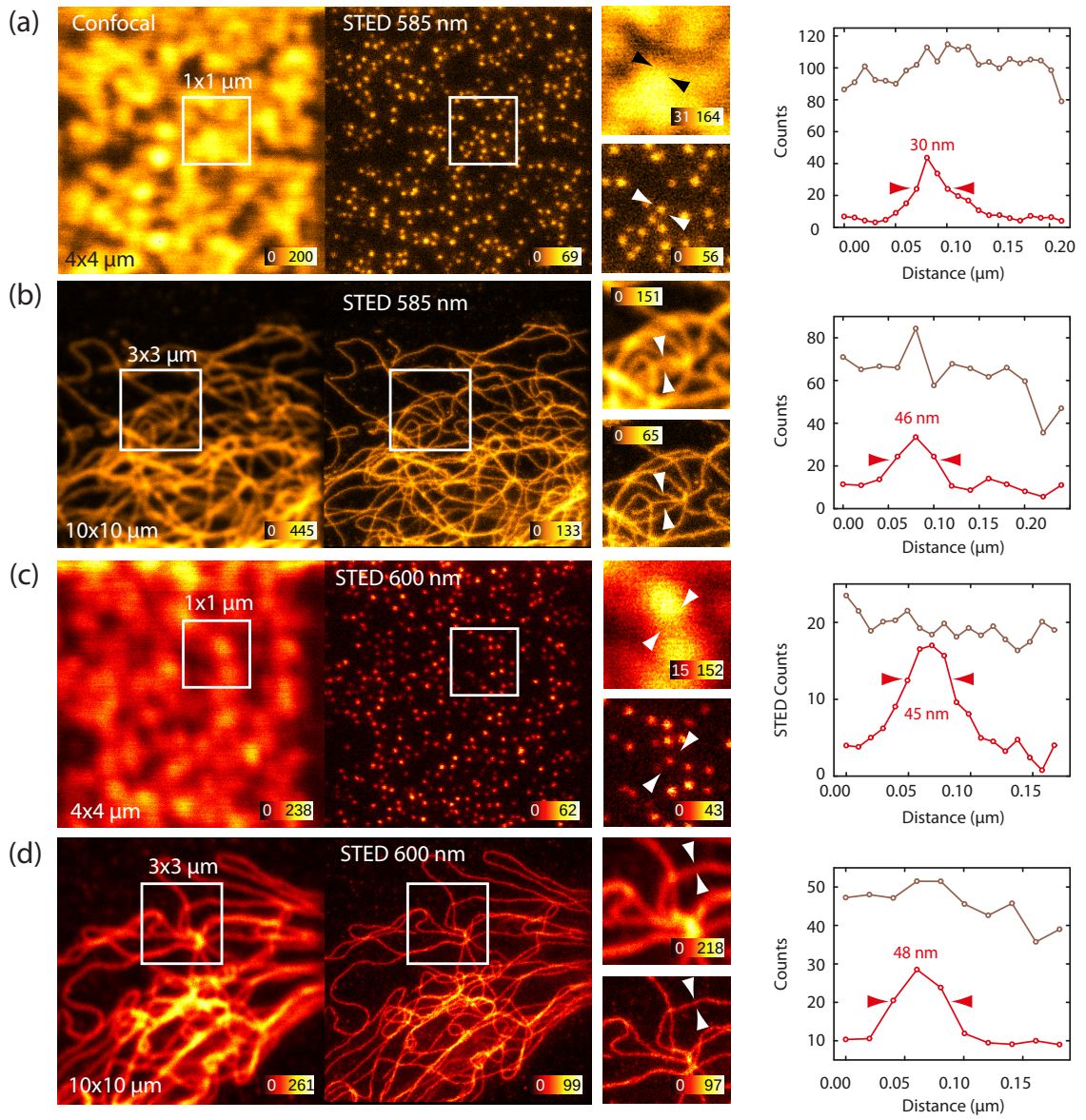

Figure 4.7: STED images taken using the 585 nm and 600 nm Stokes lines as the STED light, with corresponding confocal images at left. (a) Images using 585 nm STED light of yellow-green fluorescent nanospheres 43 nm in diameter. Intensity profiles are taken at sample position specified by the arrows. (b) Vimentin fibers labeled with Chromeo 488 in PtK2 cells. (c) Images using 600 nm STED light, also with 43 nm yellow-green nanospheres, and (d) vimentin fibers labeled with Chromeo 488. All images show the full dynamic range of the photon counts contained within each pane. The color map corresponding to the number of photon counts is shown in the bottom right of each image pane.

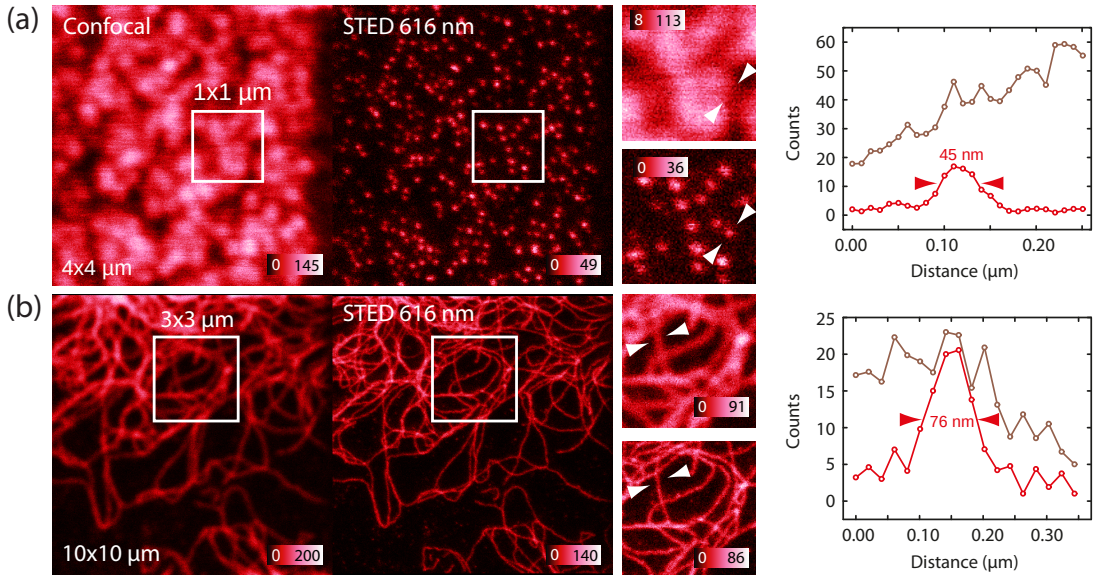

Figure 4.8: Images taken using 616 nm as STED light, with corresponding confocal images at left. (a) Yellow-green fluorescent nanospheres 43 nm in diameter. Intensity profiles are taken at sample position specified by the arrows. (b) Images of vimentin fibers labeled with Chromeo 488 in PtK2 cells. All images show the full dynamic range of the photon counts contained within each pane.

the assumption that the object and point spread functions are Gaussians, the effective point spread function of 40 nm was calculated.

4.3 20 MHz MOPA Fiber Laser Pump Source

The output repetition rate of a MOPA source is largely independent of the other laser parameters and is determined by the electronic control of the master oscillator, so to increase the pump repetition rate and the image acquisition speed, the MOPA fiber laser system was modified with new seed source electronics to support a repetition rate of 20 MHz (Mobius Photonics, Mountain View, CA, USA), a factor of one thousand faster than the original microchip laser pump source. The pulse length was shorted via the master-oscillator seed source from 2 ns to 700 ps to raise the pulse peak power and increase the conversion efficiency of SRS. At 20 MHz the 3.3 W of average power at 530 nm was provided.

Due to the lower pulse energies available from the pump laser at 20 MHz, fiber transmission losses due to photodarkening precluded the generation of the desired SRS spectrum with GeO_2:SiO_2 fiber cores. By switching to fibers with a pure silica core photodarkening was avoided. A 100 m length of S630-HP fiber from Nufern (East Granby, CT, USA) was used. The SRS spectrum used for measurements is shown in Fig. 4.9. To increase spectrum stability, the 530 nm pump light was circularly polarized. A shutter was installed before the fiber coupling to block the pump when STED light was not needed for imaging or system alignment. With these measures the fiber lifetime was increased to several months.

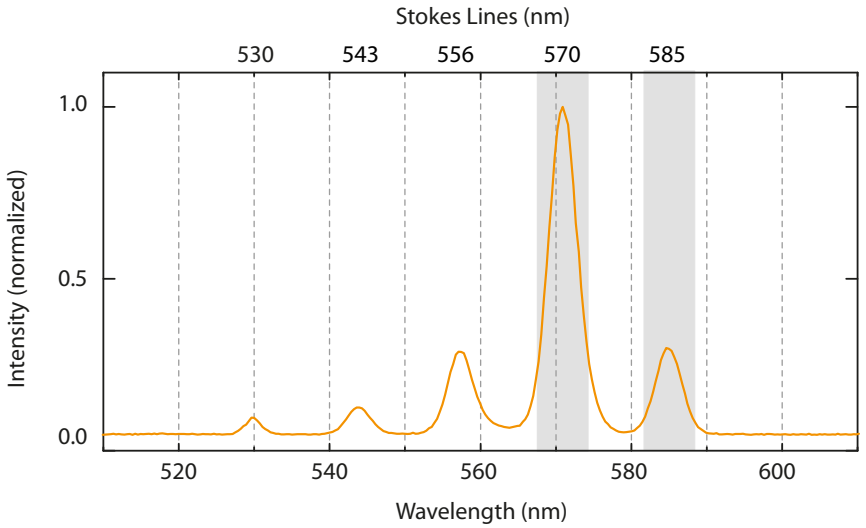

Figure 4.9: SRS spectrum created by a 100 m length of S630-HP Nufern (East Granby, CT, USA) fiber with a 530 nm pump source (Mobius Photonics, Mountain View, CA, USA), used for measurements at 20 MHz. The Stokes lines used as STED light, at 570 nm and 585 nm, are indicated by gray bars.

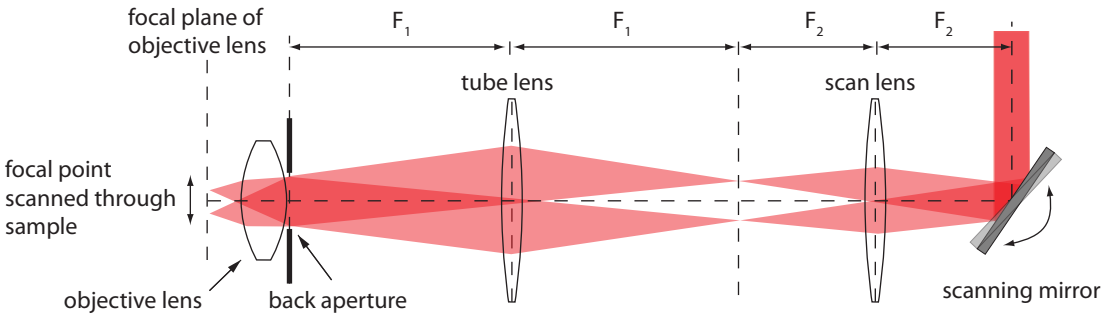

Figure 4.10: A 4F lens configuration was used to implement beam scanning. A scan and tube lens (Leica Microsystems, Mannheim, Germany) arranged in a 4F configuration allowed the beams to be scanned via two galvanometric mirrors contained in the Janus III scan head (TILL Photonics, Munich, Germany) such that both beams were scanned together through the sample in the x and y directions. In the figure only one scanning mirror is shown for simplicity. For two scanning mirrors, additional optics are required (located in the scanner) to ensure the proper conjugation of both scanning mirrors in the back aperture of the objective lens. The excitation and STED beams remain stationary in the back aperture of the objective lens. Were this not the case, not only would the excitation and STED light intensities vary as the beams were scanned due to clipping by the back aperture, but shifting the helical phase pattern of the STED beam in the back aperture would destroy the quality of the STED zero intensity spot, reducing the STED image resolution and brightness. The detected fluorescence light is de-scanned by the 4F configuration so the moving spot of fluorescence in the sample is rendered stationary for the confocal pinhole.

Beam Scanning

The 20 MHz repetition rate of the pump laser increased the image acquisition time of the system sufficiently to make a beam scanning viable. For fast image acquisition beam scanning is superior to stage scanning. The only mass accelerated during beam scanning is that of the scanning mirrors, in contrast to stage scanning, which requires the acceleration of the greater mass of the sample and scanning stage. Particularly when imaging live cells, the movement of the sample during fast stage scanning can be problematic and perturb the sample.

A 4F lens configuration, shown schematically in Fig. 4.10, consisting of a scan and a tube lens (Leica Microsystems, Mannheim, Germany), together with a Janus III scan head (TILL Photonics, Munich, Germany) was used to scan the excitation and STED beams in the focal plane of the objective lens while holding the beams fixed in the back aperture of the objective lens. Fluorescence light was de-scanned through the lens configuration, maintaining proper alignment of the excitation focal spot with the detection pinhole.

The system enabled the realization of image acquisition times on the order of a minute for images $\sim$10 µm on a side, with pixel dwell times chosen for sufficient photon counts to yield suitable images, typically 70 µs, making the system suitable for imaging slow-moving structures of live cells.

Fixed *E. coli* cells with GFP

Escherichia coli is a robust, ubiquitous bacterium and an important prokaryotic model system. The structure and function of bacterial cytoskeletal structures is of current interest [69]. In the samples imaged the FtsZ ring protein, involved in mechanically constricting the cell during cell division, was fused with GFP [70]. The FtsZ-GFP fusion protein was intentionally expressed beyond physiological conditions, which can be seen by the fact that many cells posses several FtsZ rings along the length of the cell. A STED image of several cells is shown in Fig. 4.11 with the corresponding confocal image for comparison. Areas of interest are enlarged. In inset (d), the STED image clearly reveals the twist of the ring protein in the imaging plane.

4.4 Live Cell Imaging with Fluorescent Proteins

STED imaging of live cells has been previously demonstrated with GFP [71], YFP [31], and Citrine [30, 26], a YFP variant [72]. Using the SRS light source in combination with beam scanning, both GFP and Citrine were used to obtain sub-diffraction resolution images of several structures in live mammalian cells and live yeast, proving the viability of the SRS light source for STED imaging with fluorescent proteins.

The importance of the results with GFP reported in this thesis must be emphasized. Though previous work obtained sub-diffraction images of GFP-labeled structures in cells, successful imaging was restricted to exceptionally bright structures or structures which were rapidly replenished with fresh GFP proteins, such as the endoplasmic reticulum [71]. Better imaging results with STED were obtained using Citrine and YFP. The following measure-

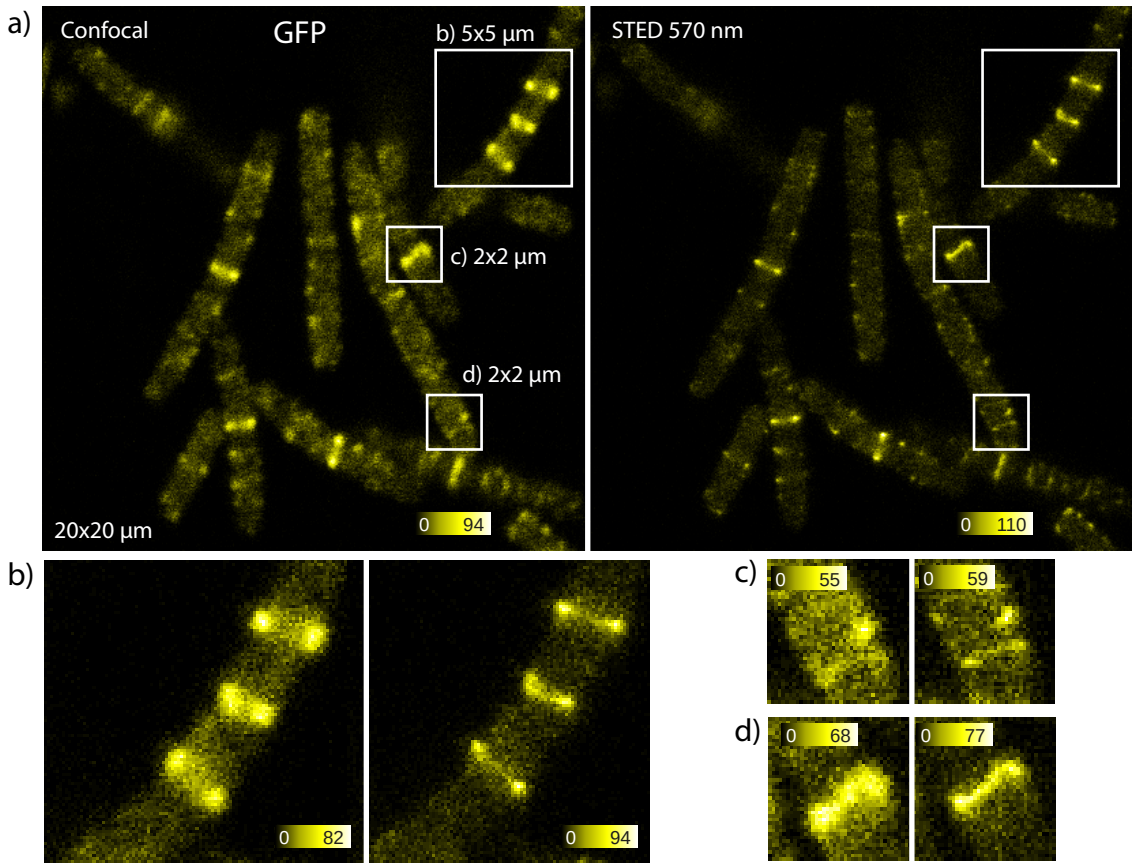

Figure 4.11: Fixed *E. coli* bacteria which, when living, expressed GFP on the FtsZ ring protein, which forms a corkscrew-like structure that encircles the middle section of the cells. 590 nm light was used for excitation. For STED light the 570 nm Stokes line was used. The excitation and STED powers used were 10 µW and 5 nW, respectively (20 MHz repetition rate). The ring protein structure can be seen more clearly in the STED images. Particularly in pane (d), the twist in the ring protein can be seen which results in the spiral structure around the cell. Note that STED images are brighter than their confocal counterparts. This effect is observed when fluorophores are so densely packed that they quench their nearest neighbors upon excitation. When some of the fluorophores are bleached, the image brightness increases because the nearest-neighbor quenching is reduced. Due to GFP overexpression the *E. coli* exhibit structure different than that of normal, healthy cells. DABCO (Roth, Karlsruhe, Germany) was added to the Mowiol (Höchst, Frankfurt, Germany) mounting medium to increase GFP photostability.

ments demonstrate that STED imaging with GFP can be performed with the same success as with Citrine- and YFP-labeled structures.

Mammalian Cells

Live cells from the mammalian PtK2 cell line (*Potorous tridactylus* kidney cells) were used as samples. STED images of three different cell structures are shown. In Fig. 4.12 measurements of keratin fibers, constituents of the cytoskeleton [73], expressing enhanced GFP (EGFP), are shown. Fig. 4.13 contains images of EGFP-labeled caveolae, invaginations 50-100 nm in size on the cell membrane, which are involved in cell signaling [74]. Tubulin fibers, also constituents of the cytoskeleton, labeled with Citrine, a YFP variant, are shown in Fig. 4.14. Cells expressing GFP were imaged using the 570 nm Stokes line for STED light; citrine samples were imaged using 585 nm STED light.

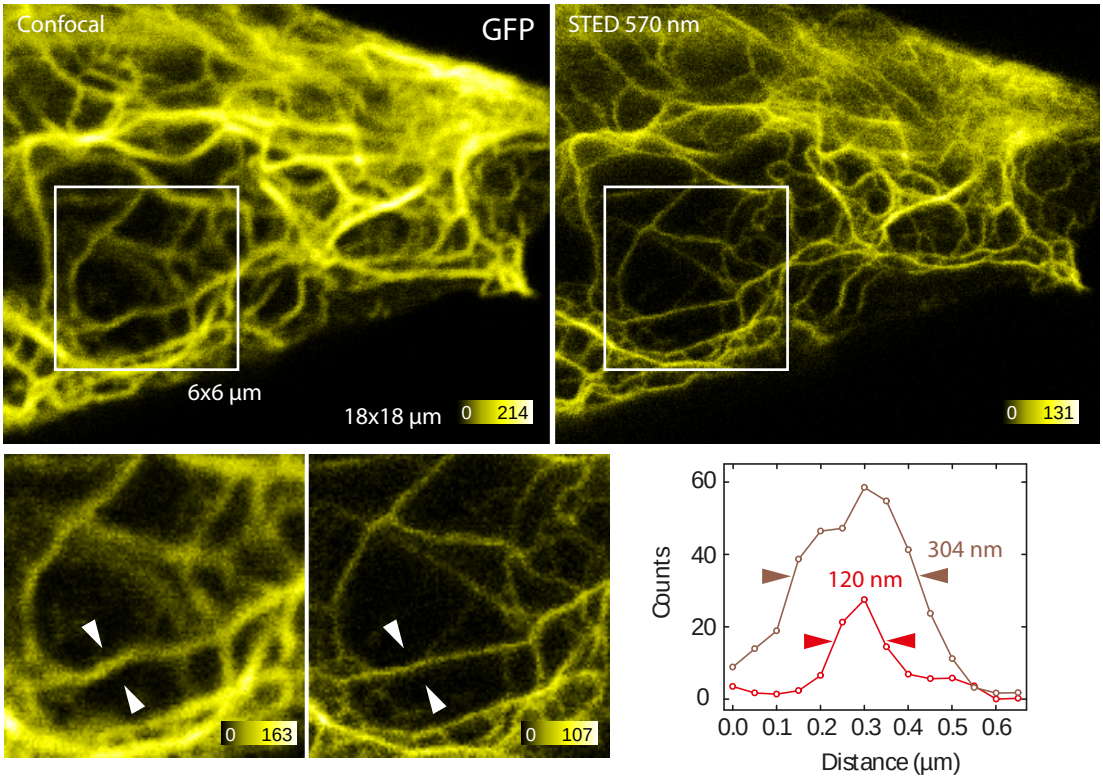

Figure 4.12: Live PtK2 cells expressing EGFP on keratin fibers. The STED wavelength was chosen as 570 nm, excitation 488 nm. The applied excitation and STED powers were 4 µW and 3.5 mW, respectively. A Pixel size 50 nm was used for both imaging modes, with a pixel dwell time of 0.07 ms for both imaging modes. All data is raw and each panel shows the complete dynamic range contained in the image.

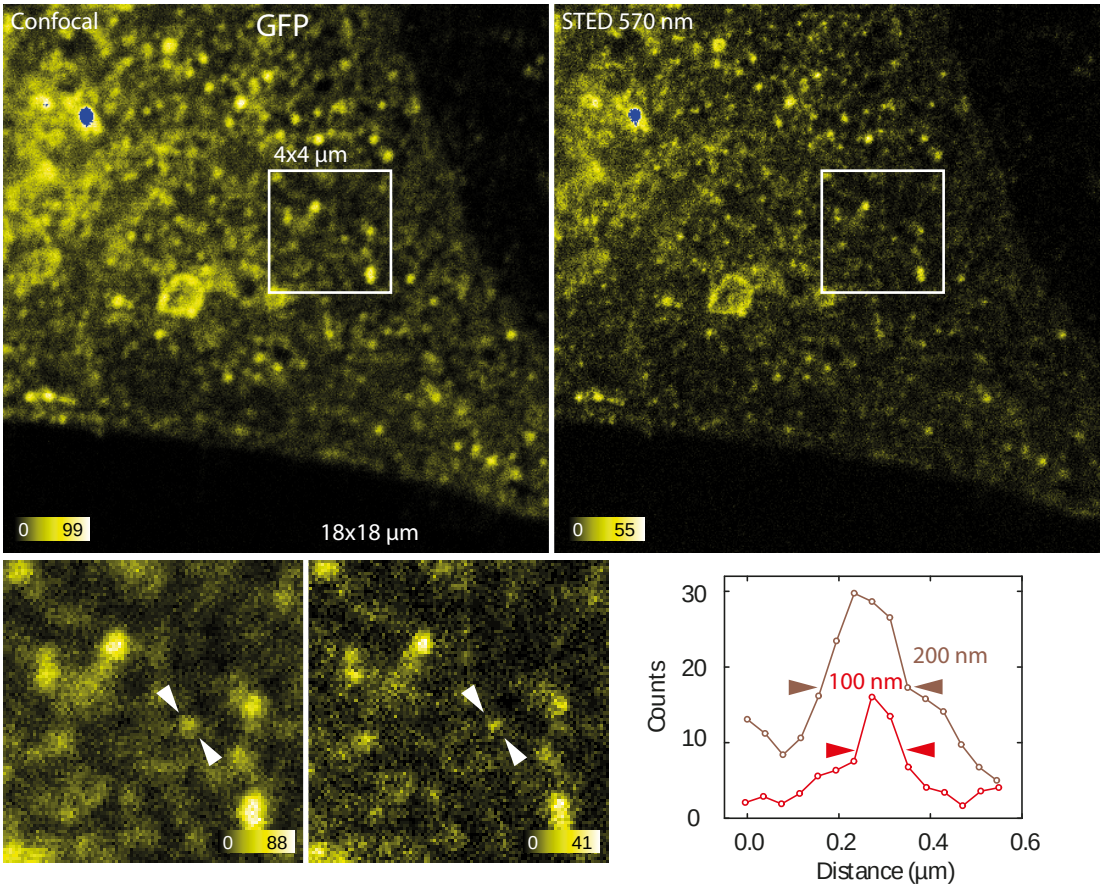

Figure 4.13: Live PtK2 cells expressing EGFP on caveolae, invaginations 50-100 nm in size in the cell membrane. Images were obtained with an excitation wavelength of 488 nm and a STED wavelength of 570 nm. The applied excitation and STED powers were 2 µW and 2 mW, respectively. Pixel sizes of 50 nm were used with pixel dwell times of 0.07 ms. All data is raw and each panel shows the complete dynamic range contained in the image, except in the blue areas of the large image panes where the photon counts are clipped so the dynamic range in the remaining image areas can be better seen.

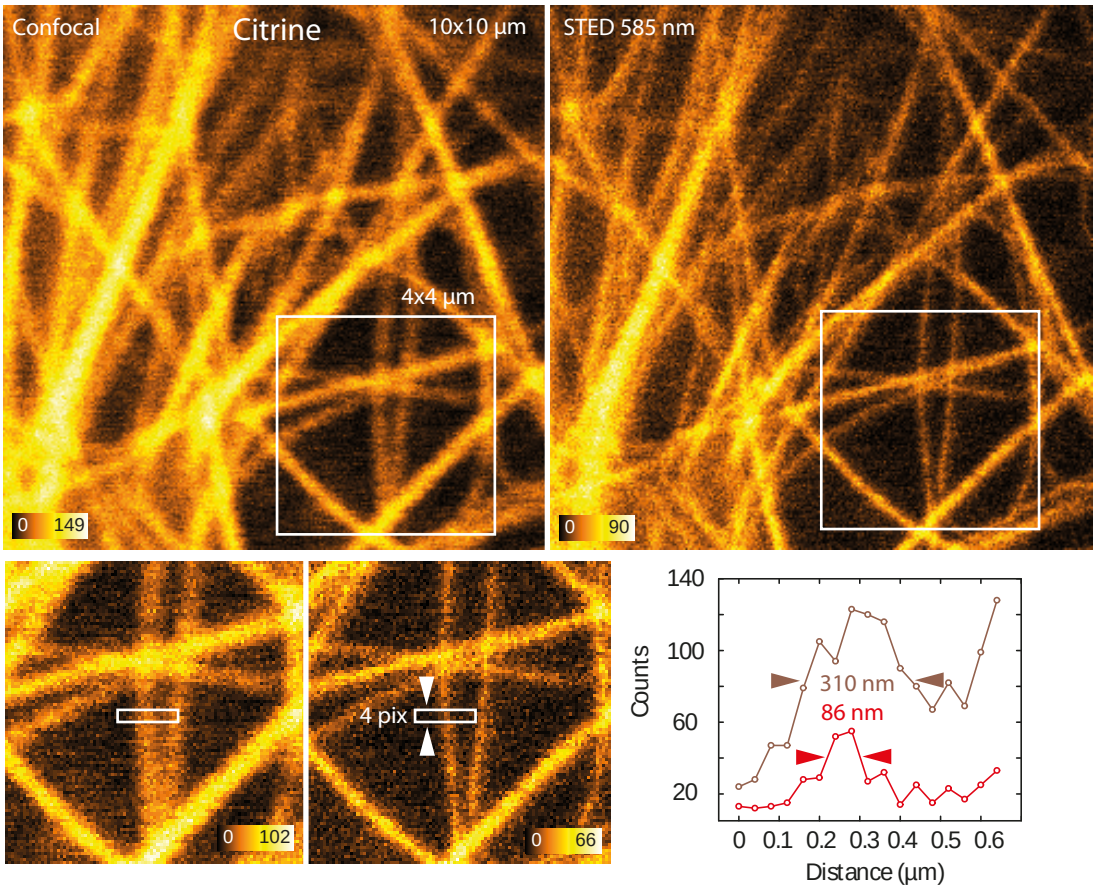

Figure 4.14: Live PtK2 cells expressing Citrine, a YFP variant, on tubulin fibers. Images were obtained with an excitation wavelength of 488 nm and a STED wavelength of 585 nm. The applied excitation and STED powers were 2 µW and 2.5 mW, respectively. Pixel sizes of 50 nm were used with pixel dwell times of 0.07 ms. The line profiles for the confocal and corresponding STED image were obtained by summing the pixels along the vertical axis of the image shown by the white box to average over noise to obtain a more reliable estimation of the resolution. All data is raw and each panel shows the complete dynamic range contained in the image.

Yeast

Baker's yeast, *Saccharomyces cerevisiae*, is the simplest eukaryotic model system. Yeast cells are robust, easy to care for, grow and reproduce quickly, and possess a relatively simple genetic structure that lends itself to easy manipulation. Importantly, being eukaryotes, they share many of the cell structures and cellular mechanics of mammalian cells. STED imaging with GFP-fusion proteins in yeast is facilitated by an extensive library of yeast clones [75]. This ready-to-use library, in combination with the ease of handling yeast cells, makes yeast an attractive subject for rapid, sub-diffraction resolution imaging of GFP with STED using the SRS light source.

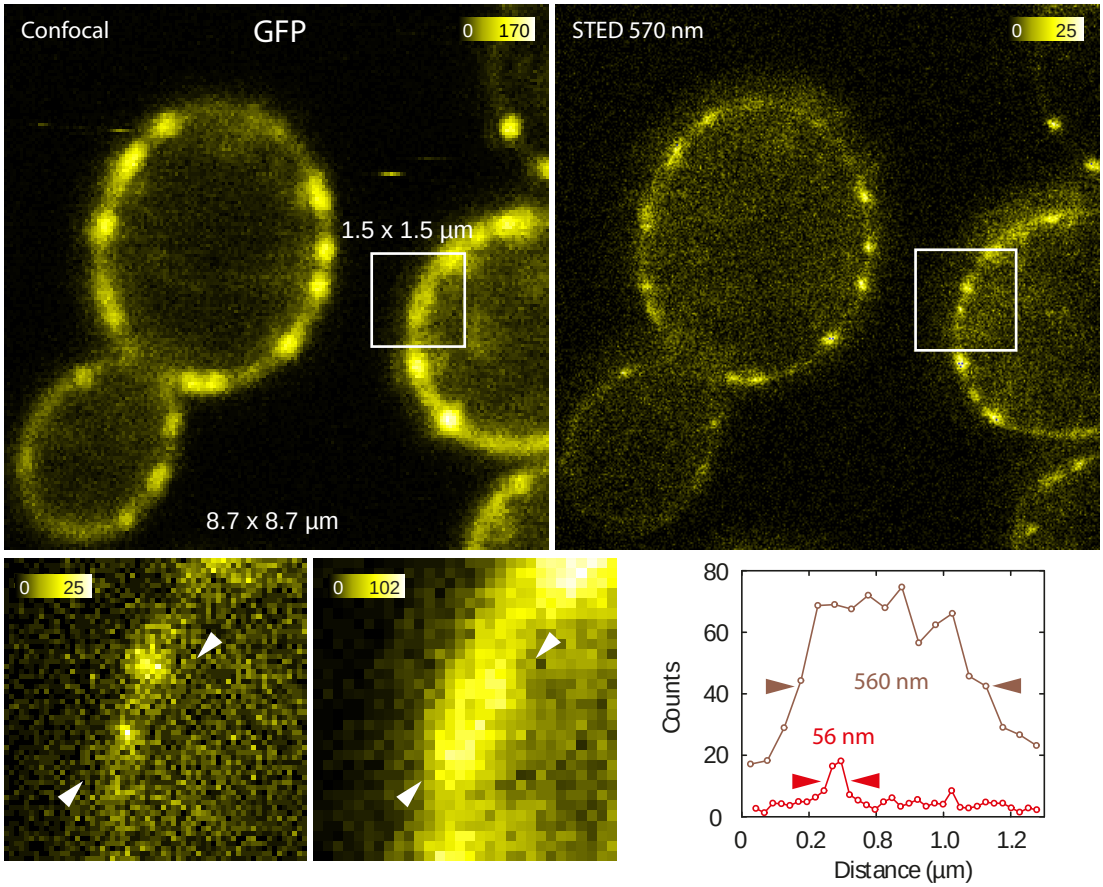

Figure 4.15: Live yeast cells expressing GFP on eisosomes. According to electron microscopy measurements eisosomes have a diameter of ∼50 nm [76]. Images were obtained with an excitation wavelength of 488 nm and a STED wavelength of 570 nm. The applied excitation and STED powers were 6 µW and 8 mW, respectively. Pixel sizes of 50 nm and 25 nm were used for confocal and STED imaging modes, respectively. Pixel dwell times of 0.07 ms and 0.1 ms were used for confocal and STED. All data is raw and each panel shows the complete dynamic range contained in the image.

Eisosomes, protein assemblies in the plasma membrane which determine the site of endocytosis, labeled with GFP were imaged [77, 78, 79, 76]. STED and corresponding confocal images are shown in Fig. 4.15 and show eisosome structures with FWHM values below 60 nm. According to electron microscopy measurements [76] eisosomes have a diameter of $\sim$50 nm.

5 Conclusion and Outlook

Live-cell microscopy using fluorescent fusion proteins is a crucial observational tool in cell biology. With STED microscopy, cellular structure and dynamics can be observed on the nanoscale unhindered by the diffraction limit of focused light. Appropriate light sources are required, however, which produce light with intensities capable of switching the fluorophores to their ground state via stimulated emission within the excited-state lifetime. The prominent role played by fluorescent proteins as markers in cell biology, namely GFP, requires a STED source in the yellow-orange range of the visible spectrum, roughly in the range from 560 to 600 nm. Tunable light sources in this range, namely a titanium:sapphire laser pumping an optical parametric oscillator (OPO), often require careful adjustment and optimization. The skill and time required to maintain such a light source for STED microscopy creates a practical barrier for implementing the technique in this spectral region. Alternatively, convenient single-color fiber laser sources are available producing suitable continuous wave light in this spectral region. Such sources are not currently spectrally tunable, however, and spectral flexibility is a great asset in STED imaging for optimizing image quality in a range of samples. Because supercontinuum fiber lasers generate broad spectral output, they have low pump conversion efficiencies to narrow wavelength ranges, ultimately constraining the repetition rate and output power within a narrow spectral range.

The goal of the work described in this thesis was to implement a simple light source for STED, offering spectral flexibility in the yellow-orange spectral range, and demonstrate its viability for live cell imaging with fluorescent proteins, especially GFP. Stimulated Raman scattering (SRS) in standard optical fibers was used to spectrally shift high-energy pulses of green light into yellow, orange, and red light with high pulse energies. The spectrally shifted light consists of discrete Stokes lines, spaced at regular frequency intervals of 13.2 THz, determined by the optical phonon spectrum of silica, the chief material of the fiber core.

First, a diode-pumped, solid state microchip laser with a kHz repetition rate and 1 ns pulses with 500 nJ pulse energy was used to create the SRS spectrum in fibers. STED imaging was demonstrated using the 532 nm pump wavelength in addition to the 588 nm, 604 nm, and 620 nm Stokes lines as STED light. Resolutions of 60-80 nm were achieved with fluorescent nanoparticles. The slow repetition rate of the pump source resulted in long imaging acquisition times, precluding practical use of the source.

A fiber laser with master-oscillator, power amplifier (MOPA) architecture was then used as the green pump source, producing 2 ns pulses with 10 μJ of energy at a repetition rate of 1 MHz. A resolution of 20-30 nm was obtained with fluorescent nanoparticles and a slightly lower resolution of 40 nm was reached in fixed cells immuno-labeled with Chromeo 488 using the Stokes lines from the fiber at 585 nm, 600 nm, and 616 nm. An improvement in both image quality and imaging speed was achieved.

To viably implement imaging of live cells using beam scanning, the repetition rate of

the MOPA pump laser was increased to 20 MHz. The pump pulse energy fell to 150 nJ as a result, but was still sufficient for the generation of the SRS Stokes lines. STED images with sub-diffraction resolution were obtained of cells expressing both green fluorescent protein (GFP) and Citrine, a yellow fluorescent protein (YFP) variant, using the 570 nm and 585 nm Stokes lines for STED, respectively. Using fixed *E. coli* cells, sub-diffraction imaging of FtsZ-GFP ring proteins was performed. Images with YFP-fusion proteins incorporated into tubulin fibers were obtained in live mammalian (PtK2) cells. Live PtK2 cells with GFP-fusion proteins in both keratin fibers and caveolae were recorded. GFP-labeled eisosomes of live yeast cells were also imaged, yielding FWHM values of eisosomes of less than 60 nm in STED images. For comparison, electron microscope images reveal eisosome diameters of $\sim$50 nm.

Continuing Live Cell STED Imaging with GFP Fusion Proteins

STED images with GFP have been obtained previously [71], but, until now, greater success with fluorescent proteins has been achieved using YFP and its variants, namely Citrine [30, 31, 26]. Measurements presented in this thesis suggest that, with the proper light source, STED images using GFP can be obtained of comparable quality to those made with YFP and Citrine. Innumerable clones of a wide range of model-system organisms are engineered with GFP-fusion proteins which now provide ready subjects for STED imaging. A next step is to begin leveraging the substantial libraries of GFP-fusion proteins for various model organisms for obtaining high resolution STED images.

Infrared SRS Spectrum Generation with Subsequent SHG

Additionally, the SRS light source will be improved [80]. An approach which may provide a solution to the problem of the limited fiber lifetime when generating the SRS spectrum in the visible is to instead generate the spectrum in the IR, at the fundamental wavelength of the pump laser, since damage thresholds for optical fiber are higher in this spectral region, and select a given Stokes line for second harmonic generation (SHG) into the visible. A complication of using single-pass SRS generation in fiber is the spectral broadening of the Stokes lines, rendering the bandwidth of light within a single Stokes line too broad for efficient SHG. This problem can be overcome by creating a fiber resonator, placing fiber Bragg gratings at two ends of a length of fiber which reflect the selected Stokes lines for amplification in the resonator. Each of the Stokes lines so produced would then be frequency doubled by an appropriate frequency doubling crystal, for example a periodically-poled lithium niobate (PPLN) waveguide of the proper poling frequency.

SRS Spectrum Seeding

Another possibility for improvement is to seed SRS spectral generation with a second light source. The stimulated scattering process is driven by the presence of photons at the Stokes frequency which are initially created by spontaneous Raman scattering in the initial length of fiber. By injecting the fiber with light red-shifted relative to the pump, at the proper

wavelength, even at low intensities, the stimulated process would be made more efficient. Perhaps pump intensities could then be reduced, relaxing the requirement for a powerful pump source and eliminating fiber damage.

A Appendix

A.1 Fiber Damage Mechanisms

High optical intensities in optical fibers can induce a variety of types of damage. The type of damage caused depends on the peak power, the wavelength of light used, pulse length, fiber type and material of the fiber. The following discussion considers the damage mechanisms observed with ∼530 nm pump light with 700 ps to 2 ns pulse duration with roughly 50 to 300 nJ of pulse energy, corresponding to peak powers in the range of 50 to 300 W. The fibers used were single mode, both PM and non-PM, with either pure silica or GeO_2-doped cores.

Photodarkening

Photodarkening, also known as color center formation, photochromic damage or photo-induced absorption, is a process by which the transmission of the fiber core decreases when the fiber is subjected to high intensity light, especially if rare-earth dopants are present in the fiber core. Photodarkening is often a function of the wavelength of light used, and is more pronounced using light in the blue and green regions of the visible spectrum. The electronic structure of the initially transparent glass of the fiber core is changed by exposure to high light intensities, knocking electrons out of their original positions in the glass structure. The electrons are bound to positively charged electron holes in the glass, and have energy levels and associated absorption spectra [81]. The index of refraction of the core can change [82], upsetting the core-cladding index mismatch disrupting the fiber waveguide properties. Additionally, scattering centers can be created. Fiber transmission losses due to photodarkening can reduce the transmitted power in the fiber to a fraction of the initial value after several hours of exposure to high intensity light. Photodarkening has been studied extensively in a variety of glass types, including GeO_2:SiO_2 [83, 84, 85, 82, 86, 87, 88], P_2O_5:SiO_2 [89], and Yb:SiO_2 [90].

Photodarkening was clearly observed in all fibers with GeO_2:SiO_2 core composition used for measurements in this thesis. When subjected to high energy 530 nm pulses, the transmission of the fibers dropped precipitously in the initial hours of operation.

Polarization Induced Birefringence

If the light intensities are high enough, the electric field strength can permanently change the mechanical stresses of the glass core, either disrupting the birefringence of PM fibers or imprinting birefringence in non-PM fibers. This effect is known as polarization-induced birefringence (PIB) [91, 92, 93, 94, 95, 96, 97, 98].

In the course of experiments for this thesis, the loss of polarization-maintaining properties of PM fibers was observed. After a period of time depending on the repetition rate of the laser and the pulse energies used, the light output of the fiber became unstable, and the polarization orientation of the light would flop between the fast and slow axes of the fiber. The effect was observed in both GeO_2:SiO_2 and pure SiO_2 core PM fibers. A change in the polarization behavior of non-PM, pure silica core fibers was also observed after transmitting light which was linearly polarized when coupled into the fiber. The non-PM fibers would begin to behave as weakly PM fibers.

Second Harmonic Generation via Periodic Poling

An additional possible source of photodamage observed during work for this thesis is second harmonic generation (SHG) within the fiber. Normally silica is a medium incapable of supporting SHG, as SiO_2 is a symmetrical molecule and the silica glass structure possesses inversion symmetry, meaning that the second-order susceptibility $\chi^{(2)}$ is zero [42]. Non-zero values of $\chi^{(2)}$ are required for SHG. However, the creation of a periodic refractive index variation in the fiber when subjected to high intensities, due to photosensitivity resulting from dopants, can imprint the fiber with a nonvanishing $\chi^{(2)}$ and leads to SHG [99, 100, 101].

If SHG took place in fibers transmitting high power light at 530 nm the doubled light would be in the UV, which is absorbed strongly by silica. The 265 nm light would therefore be difficult to observe. The strong absorption of 265 nm light by the glass could be an additional source of damage.

SHG was easily observed in single mode fibers transmitting high power nanosecond pulses of 1060 nm light [102], as the 530 nm light produced by SHG in this case is easily visible to the human eye, but the high intensity IR pump wavelength is not. This observation was made using a laser nearly identical to that used as the pump source for MHz SRS experiments in this thesis except that that output was not doubled to 530 nm.

A.2 Minimizing Fiber Damage

Fiber damage is a function of the pulse power and the number of pulses to which the fiber is exposed. By holding pulse parameters constant and increasing the repetition rate of the laser, rates for critical fiber damage were increased. As the pump laser repetition rate was increased from kHz to MHz, the fiber lifetime became a critical issue.

kHz

Using the kHz DPSS microchip laser as the pump source, the SRS fiber was subjected to pulses 1 ns in length with average pulse energies of 500 nJ (the pulse energies of the laser were bimodally distributed, with half the pulses having twice the energy of the remaining half) exiting the laser at 60 kHz. Initial fiber launch efficiencies were 50-60%. Fibers used had GeO_2:SiO_2 cores. The fiber type, CORNING PM 48-N90A from Fujikura (Tokyo, Japan) had a core diameter of 4μm and a cut-off wavelength of 410 nm. A decrease in fiber transmission due to photodarkening was observed in the initial hours of operation, with fiber transmission as a function of time following an exponential decay. After the initial decrease, however, the transmission remained stable for many months. The last Stokes lines of the SRS spectrum vanished with the initial loss of transmission, but the remaining spectrum was sufficient for STED measurements. After several months of non-continuous operation, however, the PM guidance of the fiber became unstable, presumably due to polarization-induced birefringence, and strong fluctuations in the output polarization state and the SRS comb were seen. At this point the fiber was replaced.

1 MHz

For 1 MHz experiments CORNING PM 63-U40A fiber from Fujikura (Tokyo, Japan), with a core composed of GeO_2:SiO_2 was used. The employed 530 nm pulse length was 2 ns and available pulse energy was 10 μJ, corresponding to an average power of 10 W. The spectral bandwidth of the source was < 0.5 nm. Only a fraction of the total power was used to produce the SRS spectrum used for STED measurements.

The face of the fiber was subjected to high average powers on the order of several watts. Initially serious mechanical drift of the fiber end was observed when the fiber was subjected to high launch powers, resulting in large changes in transmitted power. To increase the stability of the coupling, uncoupled waste light was allowed to dissipate in such a manner that it would not heat the fiber mount and cause drift in the fiber coupling.

Instead of being fitted with standard connectors, the fibers were left bare. The acrylate coating was stripped mechanically on the fiber ends using a razor blade, the fiber cladding was scored using the edge of a ceramic tile, and the fiber end broken off at the site of the scoring to yield a clean face free of scratches or defects. This procedure of preparing a fresh fiber face required less than a minute. For coupling, the naked fiber was then held in place opposing the objective lens using magnetic fiber clamps (Thorlabs, Newton, NJ, USA). As purchased, the clamps had teflon pads to hold the fiber in place. Due to the danger ablating the teflon with high laser power if the fiber became misaligned with the

coupling objective, the teflon pads were replaced with copper to increase thermal conduction and reduce inhomogeneities in the temperature of the holder. The fiber end was mounted to protrude from the mount by 5 to 8 mm to mitigate the heating effects of the laser light not coupled into the fiber core by reducing the incident peak light intensities falling on the mount. A piezo stage (Melles Griot, Albuquerque, NM, USA) to position the fiber after a 20× microscope objective (Olympus, Tokyo, Japan) used for launching the pump light into the fiber. This substantially reduced the time required to couple the fiber and permitted the user to optimize the coupling during high power operation.

Just as with the kHz pump source, photodarkening of the GeO_2:SiO_2 fiber core reduced fiber transmission from 50-60% to 20% in the initial hours of operation. Because of the abundance of pump power available from the laser, the losses could easily be compensated by increasing the power in the fiber. Destruction of the PM properties of the fiber was accelerated to several weeks under normal lab use.

20 MHz

With the 20 MHz MOPA pump source fiber damage became a critical issue, in large part because the pulse energies produced by the source were decreased to 150 nJ as a result of increasing the repetition rate. The extra power was no longer available to compensate for decreased fiber transmission. To raise the pulse peak power, pulses were shortened to 700 ps. The decrease in GeO_2:SiO_2 fiber transmission due to photodarkening within the span of minutes reduced the transmission below the threshold of desired SRS spectrum generation. The short usable fiber lifetime precluded the practical use of the SRS STED system, as the proportion of time spent replacing the fiber and re-aligning the STED beam exceeded the time for which STED light was provided by the fiber.

Photodarkening was circumvented by using optical fibers with a pure SiO_2 core. The initial precipitous drop in fiber transmission was no longer observed. However, polarization-induced birefringence effects became prominent, and after a short period of operation the output polarization of the fiber and SRS spectrum became unstable. In PM fibers the birefringence was destroyed, irrespective of whether the polarized input light was coupled along the fast or the slow birefringent axis, and non-PM fibers transmitting polarized pump light developed quasi-PM transmission characteristics.

Reasonable success was obtained using non-PM, pure SiO_2 fibers and carefully circularizing the polarization of the pump light before coupling into the fiber, eliminating a preferred direction for PIB effects. Additionally, a shutter was installed before the SRS fiber to block the 530 pump light and SRS spectrum generation when STED illumination was not needed, limiting the time the fiber was subjected to high intensity transmission. The combination of these two measures extended stable operation of the fiber to several months of normal measurement use.

Fiber life was still limited, however. Transmission was seen to drop gradually over weeks until the required SRS Stokes lines were no longer produced. Examination of the mode fields at both ends of the fiber indicates a destruction of the guidance properties of the fiber at the end into which the light was coupled. This observation was verified after cleaving off several centimeters of the fiber to eliminate the possibility of surface damage.

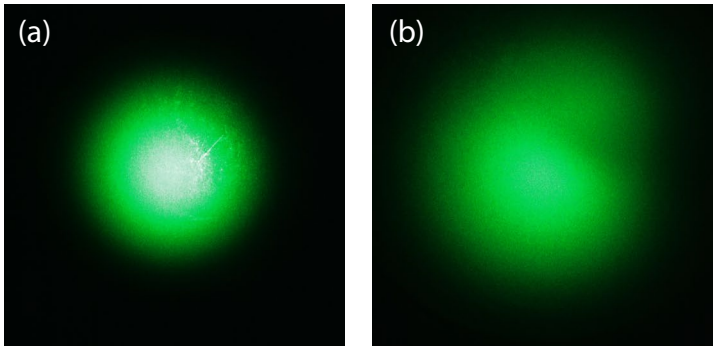

Figure A.1: Images of the mode fields exiting the two ends of a 100 m length of pure silica core S630-HP Nufern fiber (East Granby, CT, USA) after SRS spectrum degeneration. (a) shows the mode field exiting the end of the fiber which the light exits. The intensity distribution is normal for single mode operation. (b) shows the mode field of light exiting the end of the fiber used to couple the high power 530 nm pump light into the fiber. The image was made after the face of the fiber was freshly cleaved to eliminate the possibility of surface damage. Clearly the mode field is distorted as a result of damage. The relative sizes of the mode fields in the images is arbitrary; the distances between the fiber face, card, and camera were not held constant.

A comparison of the mode fields of the two fiber ends is shown in Fig. A.1. A hypothesis to explain the remaining fiber damage is that despite the measures taken, the high intensities altered the refractive index of the core, cladding, or both, leading to improper index matching resulting in transmission losses and disruption of single mode light propagation.

A.3 Sample Preparation

Fluorescent Nanospheres

Two types of fluorescent beads were used for measurements: yellow-green fluorescent nanospheres purchased from Invitrogen (Carlsbad, CA, USA), and silica beads made in-house, labeled with Atto 425 (Atto Tec, Siegen, Germany). Beads were diluted to a concentration suitable for imaging. A glass coverslide was incubated with 0.1% concentration of poly-L-lysine (Sigma-Aldrich, Steinheim, Germany) for several minutes, to promote adherence of the beads to the glass, before rinsing with distilled water. The bead solution was spread on the coverslip before again rinsing with distilled water and drying with pressurized air. Mowiol (Höchst, Frankfurt, Germany) was used as the mounting medium.

Fixed Immunostained PtK2 Samples

For the immunolabeling of vimentin, cultured cells of the mammalian cell line PtK2 (*Potorous tridactylus* kidney cells) were grown on coverslips over night. Then the cells were fixed 5 min with ice cold methanol (abs.). After washing in PBS, the samples were blocked with 5% (w/v) bovine serum albumin in PBS buffer solution and incubated with mouse monoclonal antibodies against vimentin (Santa Cruz Biotechnology, Santa Cruz, CA, USA). The primary antibodies were detected with secondary antibodies labeled with Chromeo 488 (Chromeon, Tegernheim, Germany). Finally the samples were embedded in Mowiol.

Fixed GFP *E. coli*

E. coli cells were grown either in liquid Luria-Bertani medium (LB) medium (5 g/l yeast extract, 5 g/l NaCl, 10 g/l peptone, 5 ml/l NaOH) or on respective agar plates. Antibiotics were added depending on the plasmid carried. For imaging, cells were transformed with plasmids carrying the gene for the FtsZ-GFP fusion protein; upon reaching an OD600 of 0.6, expression was induced by adding 250 µM isopropyl-thiogalactosid (IPTG, AppliChem, Darmstadt, Germany). After several hours of growth at 30°C, cells were prepared for microscopy.

Live GFP Yeast

Standard methods were used for growth and manipulation of yeast strains [103]. The yeast strain expressing the epitope-tagged fusion protein Nce102-GFP was purchased from Invitrogen (Carlsbad, USA). For imaging, yeast cells growing on agar YPD plates for 24 hours at 25°C were scraped from the plate, washed and mounted in PBS (137 mM NaCl, 3 mM KCl, 8 mM Na_2HPO_4, 1.5 mM KH_2PO_4, pH 7) immediately before imaging. Alternatively, yeast cells were grown in liquid YPD growth medium to logarithmic growth phase, being harvested by centrifugation and mounted in PBS immediately before imaging.

Live PtK2 Cells

PtK2 cells were grown as previously described [30]. Standard methods were used for cloning. To tag Keratin19 and Caveolin1 at the C-terminus with EGFP, the expression plasmids pMD-Krt19-EGFP and pMD-Cav1-GFP were constructed by Gateway vector conversion (Invitrogen, Carlsbad, CA) from the donor vectors pDONR223-Krt19 and pDONR223-Cav1, and the empty destination vector pMD-EGFP-N.

The microtubule-associated protein MAP2 was tagged at its N-terminus with Citrine. The respective plasmid was constructed by Gateway vector conversion from the donor vector pDONR223-MAP2 and the empty destination vector pSEMS-Citrine-Gateway, as described previously [32]. For transfection, PtK2 cells were grown overnight on glass coverslips. After reaching $\sim$80 % confluence, the plasmids were introduced using the Nanofectin kit according to the manufacturer's instructions (PAA, Pasching, Austria). The cells were incubated for at least 24 h before imaging.

A.4 Abbreviations

Abbreviation	Original Term
DPSS	diode-pumped, solid state (laser)
FWHM	full width (at) half maximum
GFP	green fluorescent protein
MOPA	master oscillator power amplifier
NA	numerical aperature
OPA	optical parametric amplifier
OPO	optical parametric oscillator
PIB	polarization induced birifringence
PM	polarization maintaining
PSF	point spread function
RegA	regenerative amplifier
SHG	second harmonic generation
SRS	stimulated Raman scattering
STED	stimulated emission depletion
YFP	yellow fluorescent protein

Bibliography

[1] T. Wilson and C. J. R. Sheppard. *Theory and Practice of Scanning Optical Microscopy*. Academic Press, New York, 1984.

[2] E. Abbe. Beiträge zur Theorie des Mikroskops und der mikroskopischen Wahrnehmung. *Arch. Mikr. Anat.*, 9:413–468, 1873.

[3] Lord Rayleigh. On the theory of optical images, with special reference to the microscope. *Philos. Mag.*, XLII:167–195, 1896.

[4] M. Born and E. Wolf. *Principles of Optics*. Cambridge University Press, Cambridge, 2002.

[5] W. Heisenberg. Über den anschaulichen Inhalt der quantentheoretischen Kinematik und Mechanik. *Zeitschrift für Physik*, 43:172–198, 1927.

[6] R.P. Feynman, Leighton R.B., and M. Sands. *The Feyman Lectures*. Addison-Wesley, Menlo Park, 1963.

[7] S. Hell and E. H. K. Stelzer. Fundamental improvement of resolution with a 4Pi-confocal fluorescence microscope using two-photon excitation. *Opt. Commun.*, 93:277–282, 1992.

[8] Stefan W. Hell. Far-field optical nanoscopy. *Science*, 316(5828):1153–1158, May 25 2007.

[9] Stefan W. Hell. Microscopy and its focal switch. *Nature Methods*, 6(1):24–32, Jan 2009.

[10] A. Einstein. Zur Quantentheorie der Strahlung. *Physik. Zeitschr.*, 18:121–128, 1917.

[11] A. L. Schawlow and C. H. Townes. Infrared and Optical Masers. *Phys. Rev.*, 112(6):1940–1949, Dec 1958.

[12] T. H. Maiman. Stimulated optical radiation in ruby. *Nature*, 187:121–128, 1960.

[13] J. R. Lakowicz, I. Gryczynski, J. Kusba, and V. BogdaNov. Light quenching of fluorescence: a new method to control the excited-state lifetime and orientation of fluorophores. *Photochemistry and Photobiology*, 60(6):546–562, December 1994.

[14] S. W. Hell, M. Schrader, K. Bahlmann, F. Meinecke, J. R. Lakowicz, and I. Gryczynski. Stimulated Emission on Microscopic Scale - Light Quenching of Pyridine-2 Using a Ti-Sapphire Laser. *Journal of Microscopy*, 180(Part 2):RP1–RP2, Nov 1995.

[15] I. Gryczynski, J. Kusba, Z. Gryczynski, H. Malak, and J. R. Lakowicz. Effect of fluorescence quenching by stimulated emission on the spectral properties of a solvent-sensitive fluorophore. *Journal of Physical Chemistry*, 100(24):10135–10144, June 1996.

[16] I. Gryczynski, Z. Gryczynski, and J. R. Lakowicz. Fluorescence anisotropy controlled by light quenching. *Photochemistry and Photobiology*, 67(6):641–646, June 1998.

[17] E. Rittweger, B. R. Rankin, V. Westphal, and S. W. Hell. Fluorescence depletion mechanisms in super-resolving STED microscopy. *Chemical Physics Letters*, 442(4-6):483–487, July 17 2007.

[18] O. G. Peterson, J. P. Webb, W. C. McColgin, and J. H. Eberly. Organic Dye Laser Threshold. *Journal of Applied Physics*, 42(5):1917–1928, 1971.

[19] S. E. Irvine, T. Staudt, E. Rittweger, J. Engelhardt, and S. W. Hell. Direct Light-Driven Modulation of Luminescence from Mn-Doped ZnSe Quantum Dots. *Angew. Chem.*, 47:2685–2688, 2008.

[20] S. W. Hell and J. Wichmann. Breaking the Diffraction Resolution Limit by Stimulated-Emission-Depletion Fluorescence Microscopy. *Optics Letters*, 19(11):780–782, Jun 1 1994.

[21] T. A. Klar and S. W. Hell. Subdiffraction resolution in far-field fluorescence microscopy. *Optics Letters*, 24(14):954–956, July 15 1999.

[22] V. Westphal and S. W. Hell. Nanoscale resolution in the focal plane of an optical microscope. *Physical Review Letters*, 94(14), April 2005.

[23] Benjamin Harke, Jan Keller, Chaitanya K. Ullal, Volker Westphal, Andreas Schoenle, and Stefan W. Hell. Resolution scaling in STED microscopy. *Optics Express*, 16(6):4154–4162, Mar 17 2008.

[24] Gerald Donnert, Jan Keller, Rebecca Medda, M. Alexandra Andrei, Silvio O. Rizzoli, Reinhard Luehrmann, Reinhard Jahn, Christian Eggeling, and Stefan W. Hell. Macromolecular-scale resolution in biological fluorescence microscopy. *Proceedings of the National Academy of Sciences of the United States of America*, 103(31):11440–11445, Aug 1 2006.

[25] Katrin I. Willig, Benjamin Harke, Rebecca Medda, and Stefan W. Hell. STED microscopy with continuous wave beams. *Nature Methods*, 4(11):915–918, Nov 2007.

[26] Gael Moneron, Rebecca Medda, Birka Hein, Arnold Giske, Volker Westphal, and Stefan W. Hell. Fast STED microscopy with continuous wave fiber lasers. *Optics Express*, 18(2):1302–1309, Jan 18 2010.

[27] Roman Schmidt, Christian A. Wurm, Stefan Jakobs, Johann Engelhardt, Alexander Egner, and Stefan W. Hell. Spherical nanosized focal spot unravels the interior of cells. *Nature Methods*, 5(6):539–544, Jun 2008.

[28] Roman Schmidt, Christian A. Wurm, Annedore Punge, Alexander Egner, Stefan Jakobs, and Stefan W. Hell. Mitochondrial Cristae Revealed with Focused Light. *Nano Letters*, 9(6):2508–2510, Jun 2009.

[29] Volker Westphal, Silvio O. Rizzoli, Marcel A. Lauterbach, Dirk Kamin, Reinhard Jahn, and Stefan W. Hell. Video-rate far-field optical nanoscopy dissects synaptic vesicle movement. *Science*, 320(5873):246–249, Apr 11 2008.

[30] Birka Hein, Katrin I. Willig, and Stefan W. Hell. Stimulated emission depletion (STED) nanoscopy of a fluorescent protein-labeled organelle inside a living cell. *Proceedings of the National Academy of Sciences of the United States of America*, 105(38):14271–14276, Sep 23 2008.

[31] Valentin U. Naegerl, Katrin I. Willig, Birka Hein, Stefan W. Hell, and Tobias Bonhoeffer. Live-cell imaging of dendritic spines by STED microscopy. *Proceedings of the National Academy of Sciences of the United States of America*, 105(48):18982–18987, Dec 2 2008.

[32] Birka Hein, Katrin I. Willig, Christian A. Wurm, Volker Westphal, Stefan Jakobs, and Stefan W. Hell. Stimulated Emission Depletion Nanoscopy of Living Cells Using SNAP-Tag Fusion Proteins. *Biophysical Journal*, 98(1):158–163, Jan 6 2010.

[33] L. Meyer, D. Wildanger, R. Medda, A. Punge, S. O. Rizzoli, G. Donnert, and S. W. Hell. Dual-Color STED Microscopy at 30-nm Focal-Plane Resolution. *Small*, 4(8):1095 – 1100, 2008.

[34] Dominik Wildanger, Eva Rittweger, Lars Kastrup, and Stefan W. Hell. STED microscopy with a supercontinuum laser source. *Optics Express*, 16(13):9614–9621, Jun 23 2008.

[35] D. Neumann, J. Bckers, L. Kastrup, S. W. Hell, and S. Jakobs. Two-color STED microscopy reveals different degrees of colocalization between hexokinase-I and the three human VDAC isoforms. *PMC Biophysics*, 3(4), 2010.

[36] F. Opazo, A. Punge, J. Bückers, P. Hoopmann, L. Kastrup, S. W. Hell, and S. O. Rizzoli. Limited Intermixing of Synaptic Vesicle Components upon Vesicle Recycling. *Traffic*, 11(6):800–812, 2010.

[37] B. Alberts, A. Johnson, J. Lewis, M. Raff, K. Roberts, and P. Walter. *Molecular Biology of the Cell*, page 593. Garland Science, New York, 5th edition, 2002.

[38] R. Y. Tsien. The Green Fluorescent Protein. *Annu. Rev. Biochem.*, 67:509–544, 1998.

[39] C. V. Raman. A new radiation. *Indian Journal of Physics*, 2(387), 1928.

[40] C. V. Raman and K. S. Krishnan. A New Type of Secondary Radiation. *Nature*, 121(3048):501–502, March 1928.

[41] R. H. Stolen. Nonlinearity in Fiber Transmission. *Proc. IEEE*, 68(10):1232–1236, 1980.

[42] Govind P. Agrawal. *Nonlinear Fiber Optics*, pages 316–369. Academic Press, San Diego, 1995.

[43] W. D. Johnston and I. P. Kaminow. Temperature Dependence of Raman and Rayleigh scattering in $LiNbO_3$ and $LiTaO_3$. *Phys. Rev.*, 178:1528, 1969.

[44] R. H. Stolen, A. R. Tynes, and E. P. Ippen. Raman Oscillation in Glass Optical Waveguide. *Applied Physics Letters*, 20(2):62–64, 1972.

[45] Y. R. Shen. *The Principles of Nonlinear Optics*, pages 159–163. John Wiley and Sons, New York, 1984.

[46] E. J. Woodbury and W. K. Ng. Ruby Laser Operation in Near IR. *Proceedings of the Institute of Radio Engineers*, 50(11):2367, 1962.

[47] N. Bloembergen. The Stimulated Raman Effect. *American Journal of Physics*, 35(11):989–1023, 1967.

[48] Robert W. Boyd. *Nonlinear Optics*, pages 365–389. Academic Press, San Diego, 1992.

[49] R. H. Stolen, C. Lee, and R. K. Jain. Development of the Stimulated Raman-Spectrum in Single-Mode Silica Fibers. *Journal of the Optical Society of America B-Optical Physics*, 1(4):652–657, 1984.

[50] R. W. Hellwarth. Theory of Stimulated Raman Scattering. *Physical Review*, 130(5):1850–1852, June 1963.

[51] R. G. Smith. Optical Power Handling Capacity of Low Loss Optical Fibers as Determined by Stimulated Raman and Brillouin Scattering. *Applied Optics*, 11(11):2489–2494, 1972.

[52] P. J. Gao, C. J. Nie, T. L. Yang, and H. Z. Su. Stimulated Raman-Scattering up to 10 Orders in an Optical Fiber. *Applied Physics*, 24(4):303–306, 1981.

[53] G. Rosman. High-Order Comb Spectrum from Stimulated Raman-Scattering in a Silica-Core Fiber. *Optical and Quantum Electronics*, 14(1):92–93, 1982.

[54] H. Takahashi, J. Chang, K. Nakamura, I. Sugimoto, T. Takabayashi, A. Oyobe, and Y. Fujii. Efficient single-pass Raman generation in a GeO_2 optical fiber and its application to measurement of chromatic dispersion. *Optics Letters*, 11(6):383–385, 1986.

[55] R. H. Stolen and Chinlon Lin. Self-phase-modulation in silica optical fibers. *Phys. Rev. A*, 17(4):1448–1453, Apr 1978.

[56] A. M. Weiner, J. P. Heritage, and R. H. Stolen. Self-Phase Modulation and Optical Pulse Compression Influenced by Stimulated Raman Scattering in Fibers. *Journal of the Optical Society of America B-Optical Physics*, 5(2):364–372, 1988.

[57] K. O. Hill, D. C. Johnson, B. S. Kawasaki, and R. I. MacDonald. CW 3-Wave Mixing in Single-Mode Optical Fibers. *Journal of Applied Physics*, 49(10):5098–5106, 1978.

[58] A. Saissy, J. Botineau, A. Azema, and F. Gires. 3-Wave Stimulated Raman Diffusion in Optical Fiber. *Applied Optics*, 19(10):1639–1646, 1980.

[59] J. Botineau and R. H. Stolen. Effect of Polarization on Spectral Broadening in Optical Fibers. *Journal of the Optical Society of America*, 72(12):1592–1596, 1982.

[60] R. H. Stolen and A. M. Johnson. The Effect of Pulse Walkoff on Stimulated Raman-Scattering in Fibers. *IEEE Journal of Quantum Electronics*, 22(11):2154–2160, Nov 1986.

[61] F. L. Galeener, J. C. Mikkelsen, R. H. Geils, and W. J. Mosby. Relative Raman Cross-Sections of Vitreous SiO_2, GeO2, B_2O_3, and P_2O_5. *Applied Physics Letters*, 32(1):34–36, 1978.

[62] F. L. Galeener and J. C. Mikkelsen. Raman-Spectra and Structure of Pure Vitreous P_2O_5. *Solid State Communications*, 30(8):505–510, 1979.

[63] A. S. L. Gomes, V. L. Da Silva, J. R. Taylor, B. J. Ainslie, and S. P. Craig. Picosecond stimulated Raman scattering in P_2O_5-SiO_2 based single mode optical fibre. *Optics Communications*, 64(4):373–378, 1987.

[64] T. Mizunami, H. Iwashita, and K. Takagi. Gain Saturation Characteristics of Raman Amplification in Silica and Fluoride Glass Optical Fibers. *Optics Communications*, 97(1-2):74–78, Mar 1 1993.

[65] W. D. Johnston, I. P. Kaminow, and J. G. Bergman. Stimulated Raman Gain Coefficients for Li^6NbO_3 $Ba_2NaNb_50_{15}$ and Other Materials. *Applied Physics Letters*, 13(5):190, 1968.

[66] R. Jose and Y. Ohishi. Higher nonlinear indices, Raman gain coefficients, and bandwidths in the TeO_2-ZnO-Nb_2O_5-MoO_3 quaternary glass system. *Applied Physics Letters*, 90, 2007.

[67] T. J. Kane, L. A. Smoliar, F. Adams, M. A. Arbore, D. R. Balsley, M. Byer, G. Conway, W. M. Grossman, G. Keaton, J. D. Kmetec, M. Leonardo, J. J. Morehead, and W. Wiechmann. $>$10 watt fiber laser structure with 0.5-5 MHz repetition rate and 0.5-1.5 pulse width. In I. Miyamoto, H. Helvajian, K. Itoh, K. F. Kobayashi, A. Ostendorf, and K. Sugioka, editors, *Fifth International Symposium on Laser Precision Microfabrication*, volume 5662 of *Proceedings of the Society of Photo-Optical Instrumentation Engineers (SPIE)*, pages 496–500, 2004. 5th International Symposium on Laser Precision Microfabrication, Nara, Japan, May 11-14, 2004.

[68] M. J. Leonardo, M. W. Byer, G. L. Keaton, D. J. Richard, F. J. Adams, J. L. Nightingale, M. A. Arbore, S. Guzsella, and Smoliar L.A. Fiber amplified based UV laser source. *Proc. SPIE*, 7195:7195F, 2009.

[69] Y. Shih and L. Rothfeld. The Bacterial Cytoskeleton. *Microbiology and Molecular Biology Reviews*, 70(3):729–754, Sep 2006.

[70] D. S. Weiss, J. C. Chen, J. M. Ghigo, D. Boyd, and J. Beckwith. Localization of FtsI (PBP3) to the Septal Ring Requires Its Membrane Anchor, the Z Ring, FtsA, FtsQ, and FtsL. *Journal of Bacteriology*, 181(2):508–520, Jan 1999.

[71] K. I. Willig, S. O. Rizzoli, V. Westphal, R. Jahn, and S. W. Hell. STED microscopy reveals that synaptotagmin remains clustered after synaptic vesicle exocytosis. *Nature*, 440(7086):935–939, Apr 13 2006.

[72] O. Griesbeck, G. S. Baird, R. E. Campbell, D. A. Zacharias, and R. Y. Tsien. Reducing the environmental sensitivity of yellow fluorescent protein: Mechanisms and applications. *J. Biol. Chem.*, 276:29188–29194, 2001.

[73] J. Kirfel, T. M. Magin, and J. Reichelt. Keratins: a structural scaffold with emerging functions. *Cellular and Molecular Life Sciences*, 60:56–71, 2003.

[74] R. G. W. Anderson. The Caveolae Membrane System. *Annu. Rev. Biochem.*, 67:199–225, July 1998.

[75] W. K. Huh, J. V. Falvo, L. C. Gerke, A. S. Carroll, R. W. Howson, J. S. Weissman, and E. K. O'Shea. Global analysis of protein localization in budding yeast. *Nature*, 425:686–691, Oct 2003.

[76] V. Stradalova, W. Stahlschmidt, G. Grossmann, M. Blazikova, R. Rachel, W. Tanner, and J. Malinsky. Furrow-like invaginations of the yeast plasma membrane correspond to membrane compartment of Can1. *Journal of Cell Science*, 122(16):2887–2894, 2009.

[77] T. C. Walther, J. H. Brickner, P. S. Aguilar, S. Bernales, C. Pantoja, and P. Walter. Eisosomes mark static sites of endocytosis. *Nature*, 439(0):998–1003, Feb 2006.

[78] G. Grossmann and W. Tanner. Inseln der Ruhe in rauher See. *Biospektrum*, pages 695–697, July 2008.

[79] G. Grossmann, J. Malinsky, W. Stahlschmidt, M. Loibl, I. Weig-Meckl, W. B. Frommer, M. Opekarova, and W. Tanner. Plasma membrane microdomains regulate turnover of transport proteins in yeast. *Journal of Cell Biology*, 183(6):1075–1088, 2008.

[80] Mobius Photonics. *Personal correspondence*. Patent Pending, Mountain View, CA, USA, 2010.

[81] Neil W. Ashcroft and N. David Mermin. *Solid State Physics*. Brooks Cole, Cambridge, 1976.

[82] D. P. Hand and P. S. Russell. Photoinduced Refractive-Index Changes in Germanosilicate Fibers. *Optics Letters*, 15(2):102–104, Jan 15 1990.

[83] V. B. Neustruev. Color-Centers in Germanosilicate Glass and Optical Fibers. *Journal of Physics-Condensed Matter*, 6(35):6901–6936, Aug 29 1994.

[84] B. Leconte, W. X. Xie, M. Douay, P. Bernage, P. Niay, J. F. Bayon, E. Delevaque, and H. Poignant. Analysis of color-center-related contribution to Bragg grating formation in Ge:SiO_2 fiber based on a local Kramers-Kronig transformation of excess loss spectra. *Applied Optics*, 36(24):5923–5930, Aug 20 1997.

[85] K. O. Hill, Y. Fujii, D. C. Johnson, and B. S. Kawasaki. Photosensitivity in Optical Fiber Waveguides: Application to Reflection Filter Fabrication. *Applied Physics Letters*, 32(10):647–649, 1978.

[86] L. Dong, J. L. Archambault, L. Reekie, P. S. J. Russell, and D. N. Payne. Photoinduced Absorption Change in Germanosilicate Preforms - Evidence for the Color-Center Model of Photosensitivity. *Applied Optics*, 34(18):3436–3440, Jun 20 1995.

[87] O. M. Efimov, K. Gabel, S. V. GarNov, L. B. Glebov, S. Grantham, M. Richardson, and M. J. Soileau. Color-center generation in silicate glasses exposed to infrared femtosecond pulses. *Journal of the Optical Society of America B-Optical Physics*, 15(1):193–199, Jan 1998.

[88] L. J. Poyntzwright, M. E. Fermann, and P. S. Russell. Nonlinear Transmission and Color-Center Dynamics in Germanosilicate Fibers at 420-540 nm. *Optics Letters*, 13(11):1023–1025, Nov 1988.

[89] B. Malo, J. Albert, F. Bilodeau, T. Kitagawa, D. C. Johnson, K. O. Hill, K. Hattori, Y. Hibino, and S. Gujrathi. Photosensitivity in Phosphorus-Doped Silica Glass and Optical Wave-Guides. *Applied Physics Letters*, 65(4):394–396, July 25 1994.

[90] Joona Koponen, Mikko Soderlund, Hanna J. Hoffman, Dahv A. V. Kliner, Jeffrey P. Koplow, and Mircea Hotoleanu. Photodarkening rate in Yb-doped silica fibers. *Applied Optics*, 47(9):1247–1256, Mar 20 2008.

[91] N. F. Borrelli, C. M. Smith, J. J. Price, and D. C. Allan. Polarized excimer laser-induced birefringence in silica. *Applied Physics Letters*, 80(2):219–221, Jan 14 2002.

[92] P. Yang, G. R. Burns, J. P. Guo, T. S. Luk, and G. A. Vawter. Femtosecond laser-pulse-induced birefringence in optically isotropic glass. *Journal of Applied Physics*, 95(10):5280–5283, May 15 2004.

[93] J. Moll, D. C. Allan, and U. Neukirch. Advances in the use of birefringence to measure laser-induced density changes in fused silica. In B. W. Smith, editor, *Optical Microlithography XVII, PTS 1-3*, volume 5377 of *Proceedings of the Society of Photo-Optical Instrumentation Engineers (SPIE)*, pages 1721–1726, 2004. Conference on Optical and Microlithography XVII, Santa Clara, CA, Feb 24-27, 2004.

[94] P. Yang, D. R. Tallant, G. R. Burns, and J. P. Guo. Femtosecond laser induced structural modification and birefriengence in bulk glass for optical waveguide applications. In S. Bhandarkar, editor, *Advances in Photonic Materials and Devices*, volume 163 of *Ceramic Transactions*, pages 61–73, 2005. 106th Annual Meeting of the American-Ceramic-Society, Indianapolis, IN, Apr 18-21, 2004.

[95] U. Neukirch, D. C. Allan, N. F. Borrelli, C. E. Heckle, M. Mlejnek, J. Moll, and C. M. Smith. Laser-induced birefringence in fused silica from polarized lasers. In B. W. Smith, editor, *Optical Microlithography XVIII, Pts 1-3*, volume 5754 of *Proceedings of the Society of Photo-Optical Instrumentation Engineers (SPIE)*, pages 638–645, 2005. Conference on Optical Microlithography XVIII, San Jose, CA, Mar 01-04, 2005.

[96] Charlene M. Smith and Nicholas F. Borrelli. Behavior of 157 nm excimer-laser-induced refractive index changes in silica. *Journal of the Optical Society of America B-Optical Physics*, 23(9):1815–1821, Sep 2006.

[97] Douglas C. Allan, Michal Mlejnek, Ulrich Neukirch, Charlene M. Smith, and Frances M. Smith. Exposure and compositional factors that influence polarization induced birefringence in silica glass - art. no. 65201z. In D. G. Flagello, editor, *Optical Microlithography XX, Pts 1-3*, volume 6520 of *Proceedings of the Society of Photo-Optical Instrumentation Engineers (SPIE)*, page Z5201, 2007. Conference on Optical Microlithography XX, San Jose, CA, Feb 27-Mar 02, 2007.

[98] Takayuki Tamaki, Wataru Watanabe, and Kazuyoshi Itoh. Structural Modification in Borosilicate Glass by Use of Femtosecond Fiber Laser at 1.56 μm. *Journal of Laser Micro Nanoengineering*, 2(1):26–30, Mar 2007.

[99] M. C. Farries, P. S. J. Russell, M. E. Fermann, and D. N. Payne. 2nd-Harmonic Generation in an Optical Fiber by Self-Written Chi(2) Grating. *Electronics Letters*, 23(7):322–324, Mar 26 1987.

[100] M. V. Bergot, M. C. Farries, M. E. Fermann, L. Li, L. J. Poyntzwright, P. S. J. Russell, and A. Smithson. Generation of Permanent Optically Induced 2nd-Order Nonlinearities in Optical Fibers by Poling. *Optics Letters*, 13(7):592–594, July 1988.

[101] R. H. Stolen and H. W. K. Tom. Self-Organized Phase-Matched Harmonic-Generation in Optical Fibers. *Optics Letters*, 12(8):585–587, Aug 1987.

[102] Gregory L. Keaton and Manuel J. Leonardo. Mobius photonics. *Personal correspondence*, Mountain View, CA, 2010.

[103] F. Sherman. *Getting started with yeast. Methods in Enzymology: Guide To Yeast Genetics and Molecular and Cell Biology*. Academic Press, London, 2002.

List of Publications

Parts of this thesis have been published in the following publications:

1. Brian R. Rankin, Robert R. Kellner and Stefan W. Hell. Stimulated-emission-depletion microscopy with a multicolor stimulated-Raman-scattering light source. *Optics Letters* 33:2491-2493, 2008.

2. Brian R. Rankin, and Stefan W. Hell. STED microscopy with a MHz pulsed stimulated-Raman-scattering source. *Optics Express* 17: 15679-15684, 2009.

3. Kastrup, L., D. Wildanger, B. Rankin, and S.W. Hell. STED Microscopy with Compact Light Sources. *Nanoscopy and Multidimensional Optical Fluorescence Microscopy*, Edited by A. Diaspro, CRC Press, 2010.

Acknowledgments

I owe a debt of gratitude to the following people, who played key roles in the research which resulted in this thesis:

Stefan Hell maintained a constant willingness to pursue the project and remained supportive during times when the outlook was dire.

Dirk Dubbers kindly agreed to be a referee for this thesis.

Robert Kellner not only provided kind mentorship as I began this work, but together with Jaydev Jethwa and Torsten Staudt formulated the ansatz of using the light from the SRS comb for STED, the idea which bloomed into this doctoral thesis.

Benjamin Harke introduced me to the practical aspects of STED microscopy during my initial time in the lab and continued to provide crucial suggestions and advice during the thesis research.

Gael Moneron offered innumerable pieces of technical advice and practical strategies for problem-solving, in addition to his work screening dyes for use with STED in the range of 600 nm, from which I greatly profited.

Christian Wurm supplied biological samples and performed STED measurements on the setup, playing an important role in the GFP STED imaging experiments.

Andreas Schönle provided the software used to control hardware during measurements, Imspector, and assisted with computer issues.

Scott Irvine and Chaitanya Ullal provided advice and thoughts on numerous issues, in addition to offering valuable pointers in writing publications relevant to this thesis.

Jaydev Jethwa performed initial fiber measurements providing valuable information for the project, and was constant in his cheerful support in any technical matter whatsoever.

Christian Eggeling was always available to provide technical help and was invaluable in procuring needed equipment in a flash. (The dude abides.)

Jan Keller-Findeisen (formerly Keller) provided his program for data analysis, took the time for many helpful discussions, and provided help with LaTeX.

Marcel Lauterbach provided extensive help with the LaTeX typesetting of this thesis.

Peng Xi characterized SRS fibers for 20 MHz experiments in addition to assembling the optics for the beam scanning. His enthusiastic support sped progress significantly.

Birka Lalkens (formerly Hein) and Katrin Willig provided advice with live-cell imaging experiments using fluorescent proteins.

Rebecca Medda and Ellen Rothermel prepared fixed cells for biological images, and Tanja Gilat prepared transfected cells for live-cell imaging experiments.

Mark Bates, Ann McEvoy, and Jan Liphardt (my undergraduate research advisor!) kindly provided fixed *E. coli* samples expressing the GFP-FtsZ fusion protein for imaging experiments.

Volker Westphal lent his technical expertise on many occasions to solve problems with electronics.

Mariano Bossi fabricated silica beads impregnated with dye for the kHz STED measurements.

Harald Meyer helped with electronics and procurement of equipment.

Marco Roose offered immediate assistance when any computer issue arose, enabling me to focus more time and energy on work in the lab.

Holger Hundertmark, Alexander Podlipensky, and Philip Russell aided our attempts to use photonic crystal fiber for SRS spectrum generation. Holger provided valuable tricks for cleaving and coupling fibers, saving me innumerable hours of work.

Thanks is also due to the following people for proofreading sections of this thesis and giving helpful suggestions for improvement:

Katja Wolff

Christian Wurm

Marcel Lauterbach

Jan Keller-Findeisen

Gael Moneron

Sebastian Berning

Ilaria Testa

Errata

Page 6

I state that fluorophores relax to the lowest vibrational state in tens of picoseconds. This should read hundreds of femtoseconds.

Page 9

"This is shown in Fig. 1.6 (b)," should read "This is shown in Fig. 1.6 **(c) and (f)."**

Page 18

$$m_s(z) = m_s(0)e^{g_R z}$$

should be

$$m_s(z) = m_s(0)e^{g_R m_p z}$$

Page 24

"The Raman threshold, given by Eqn. 3.10 for the circularly polarized case is twice that of the linearly polarized case [42]."

should read

"The Raman threshold, given by Eqn. 3.10 for the **linearly polarized case, is twice that for the circularly polarized case [42]."**

Page 37

Reference [71] should be:

> K. I. Willig, R. R. Kellner, R. Medda, B. Hein, S. Jakobs, S. W Hell. Nanoscale resolution in GFP-based microscopy. *Nature Methods* 3 (9): 721-723, 2006.

I incorrectly state that live-cell STED imaging with GFP was demonstrated in reference [71] (now replaced with the above reference). The cells were fixed.

Page 38

The caption of Fig. 4.11 states that the excitation wavelength was 590 nm. This should read 490 nm.